

C-terminal residues of ferredoxin-NAD(P)⁺ reductase from *Chlorobaculum tepidum* are responsible for reaction dynamics in the hydride transfer and redox equilibria with NADP⁺/NADPH

メタデータ	言語: eng 出版者: 公開日: 2018-06-08 キーワード (Ja): キーワード (En): 作成者: メールアドレス: 所属:
URL	https://doi.org/10.24517/00049539

This work is licensed under a Creative Commons Attribution-NonCommercial-ShareAlike 3.0 International License.



C-terminal residues of ferredoxin-NAD(P)⁺ reductase from *Chlorobaculum tepidum* are responsible for reaction dynamics in the hydride transfer and redox equilibria with NADP⁺/NADPH

Daisuke Seo^{1*}, Tomoya Asano^{2,3}

¹Division of Material Science, Graduate School of Natural Science and Technology, Kanazawa University, Kakuma, Kanazawa, Ishikawa 920-1192, Japan

²Division of Functional Genomics, Advanced Science Research Center, Kanazawa University, Takaramachi 13-1, Kanazawa, Ishikawa 920-0934, Japan

³Present address: Wakasa Seikatsu Co. Ltd, 22 Naginataboko-cho, Shijo-Karasuma, Shimogyo-ku, Kyoto 600-8008, Japan.

*To whom correspondence should be addressed: Daisuke Seo

Division of Material Science, Graduate School of Natural Science and Technology, Kanazawa University, Kakuma, Kanazawa, Ishikawa 920-1192, Japan

Tel: +81-76-264-5683

Fax: +81-76-264-5742

Email: dseo@se.kanazawa-u.ac.jp

Keywords

Flavoenzyme; stopped-flow; green sulfur bacteria; charge transfer.

Abbreviations

A, absorbance; AdR, adrenodoxin reductase; *Bs*, *Bacillus subtilis*; *Ct*, *Chlorobaculum tepidum*; CT, charge transfer; CTC, charge transfer complex; *Ec*, *Escherichia coli*; FAD, flavin adenine dinucleotide; Fd, ferredoxin; FMN, flavin mononucleotide; FNR, ferredoxin-NAD(P)⁺ oxidoreductase; GR, glutathione reductase; G6P, glucose-6-phosphate; G6PDH, glucose-6-phosphate dehydrogenase; HEPES, 4-(2-hydroxyethyl)-1-piperazineethanesulfonic acid; K_d , dissociation constant; K_M , Michaelis constant; MALDI-TOF MS, matrix assisted laser dye ionization-time of flight mass spectrometry; PdR, putidaredoxin reductase; Tris, tris(hydroxymethyl)aminomethane; TrxR, bacterial NADPH-thioredoxin reductase; Suffixes: ox, oxidized; red, reduced; WT, wild type.

Acknowledgement

This work was partly supported by JSPS KAKENHI Grant Number JP17K07304 (to DS).

Abstract

Ferredoxin-NAD(P)⁺ reductase ([EC 1.18.1.2], [EC 1.18.1.3]) from *Chlorobaculum tepidum* (*CtFNR*) is structurally homologous to the bacterial NADPH-thioredoxin reductase (TrxR), but possesses a unique C-terminal extension relative to TrxR that interacts with the isoalloxazine ring moiety of the flavin adenine dinucleotide prosthetic group. In this study, we introduce truncations to the C-terminal residues to examine their role in the reactions of *CtFNR* with NADP⁺ and NADPH by spectroscopic and kinetic analyses. The truncation of the residues from Tyr326 to Glu360 (the whole C-terminal extension region), from Phe337 to Glu360 (omitting Phe337 on the *re*-face of the isoalloxazine ring) and from Ser338 to Glu360 (leaving Phe337 intact) resulted in a blue-shift of the flavin absorption bands. The truncations caused a slight increase in the dissociation constant toward NADP⁺ and a slight decrease in the Michaelis constant toward NADPH in steady-state assays. Pre-steady-state studies of the redox reaction with NADPH demonstrated that deletions of Tyr326–Glu360 decreased the hydride transfer rate, and the amount of reduced enzyme increased at equilibrium relative to wild-type *CtFNR*. In contrast, the deletions of Phe337–Glu360 and Ser338–Glu360 resulted in only slight changes in the reaction kinetics and redox equilibrium. These results suggest that the C-terminal region of *CtFNR* is responsible for the formation and stability of charge-transfer complexes, leading to changes in redox properties and reactivity toward NADP⁺/NADPH.

Introduction

Ferredoxin-NAD(P)⁺ oxidoreductase ([EC 1.18.1.2], [EC 1.18.1.3], FNR), adrenodoxin reductase ([EC 1.18.1.6], AdR) and putidaredoxin reductase ([EC 1.18.1.5], PdR) are NAD(P)H-dependent oxidoreductases in the flavoprotein superfamily that catalyze the redox reaction between the two-electron carrier nucleotides NAD(P)⁺/NAD(P)H, and the one-electron carrier iron-sulfur proteins ferredoxin (Fd), adrenodoxin, and putidaredoxin, respectively. These enzymes have a conserved protein topology composed of two nucleotide-binding domains: one for flavin adenine dinucleotide (FAD)- or flavin mononucleotide (FMN)-binding, and the other for NAD(P)⁺/NAD(P)H-binding (Aliverti et al. 2008; Dym and Eisenberg 2001). Based on amino acid sequence and structure analyses, FNR, AdR and PdR can be classified into two major categories, plant-type and glutathione reductase (GR)-type, each of which includes several subgroups (Aliverti et al. 2008; Correll et al. 1993; Karplus and Faber 2004; Ceccarelli et al. 2004; Medina and Gomez-Moreno 2004; Seo et al. 2004). The TrxR-type FNR, a subgroup of the GR-type FNR found in green sulfur bacteria, Firmicutes and several Alphaproteobacteria, is distinctive from the other types of FNR as it is a homodimer with significant conservation of structural topology with bacterial NADPH-thioredoxin reductase (TrxR) (Muraki et al. 2010; Komori et al. 2010). The crystal structures of *Chlorobaculum tepidum* FNR (*Ct*FNR, Muraki et al. 2010 [PDB code: 3AB1]), *Thermus thermophilus* HB8 thioredoxin reductase-like protein (PDB code: 2ZBW) and *Bacillus subtilis* FNR (*Bs*FNR, Komori et al. 2010 [PDB codes: 3LZX, 3LZW]) revealed stacking of aromatic residues on the *si*- and *re*-faces of the isoalloxazine ring moiety and a C-terminal extension relative to TrxR on the *re*-face of the ring. In the crystal structure of oxidized *Ct*FNR, Tyr57 and Phe337 stacked on the *si*- and *re*-faces, respectively, of the isoalloxazine ring moiety, almost in parallel, at a distance of approximately 3.5 Å from the centroid of the isoalloxazine ring. The 23 amino acid residues following Phe337 comprise the 7th α-helix of the protein, form the C-terminal extension, and are on the *re*-face of the ring (Fig. 1a, b, Muraki et al. 2010). Interestingly, similar arrangements of amino acid residue(s) around the isoalloxazine ring moiety are often found in the flavoprotein superfamily, including plant-type FNRs. In plant-type FNRs, mutations of the amino acid residues close to the *re*-face of the isoalloxazine ring moiety, including the *re*-face Tyr residue, resulted in drastic changes in the specificity, reactivity and the relative redox properties toward NAD(P)⁺/NAD(P)H (Piubelli et al. 2000; Nogués et al. 2004; Tejero et al. 2005; Lans et al. 2010; Peregrina et al. 2010; Bortolotti et al. 2014). Steady-state studies with truncations of the C-terminal extension region of *Bs*FNR, a TrxR-type FNR, revealed that the truncations had little effect on the NADPH oxidation reaction, but the rate of Fd reduction decreased drastically (Seo et al. 2014). However, the details concerning the role of the C-terminal region of the TrxR-type FNR, especially in the hydride transfer process and formation of the NAD(P)⁺/NADPH-FNR complex, remain unclear.

Recently, pre-steady-state kinetic studies of *Bs*FNR and *Ct*FNR have revealed that hydride transfer is the rate-limiting step during the NADPH oxidation reaction, and the rate constant of the hydride transfer step toward NADPH oxidation is much faster than that toward NADP⁺ reduction (500 s⁻¹ vs. <10 s⁻¹) in the case of *Bs*FNR, whereas the rate constants in both directions are comparable in the case of *Ct*FNR (Seo et al. 2016a, b). As this difference in reversibility relates to their physiological roles, a comparative study of these two FNRs would contribute to our understanding of the structure-function relationships of FNRs. In the structures of these two FNRs, there are conspicuous differences at the C-terminal extension (Fig. 1a, b), in the NADPH binding site on the surface of the NAD(P)⁺/NAD(P)H-binding domain, and in the hinge regions that connect the two nucleotide-binding domains (Muraki et al. 2010; Komori et al. 2010). The crystal structure of *Bs*FNR in the NADP⁺-bound form revealed that *Bs*FNR and *Escherichia coli* (*Ec*) TrxR share similarities in their NADP⁺ binding mode (Komori et al. 2010), leading to the idea that a drastic domain motion must occur to achieve a hydride transfer between NAD(P)⁺/NAD(P)H and the FAD prosthetic group (Waksman et al. 1994). Therefore, the above differences between *Bs*FNR and *Ct*FNR would affect the reactivity toward NADP⁺/NADPH to some extent. The C-terminal extension region would affect the close stacking of the nicotinamide ring moiety of NADP⁺/NADPH with the isoalloxazine ring moiety of FAD, thereby participating in the formation of a charge transfer complex (CTC) with NAD(P)⁺/NAD(P)H. From the alignment of the amino acid sequences of the C-terminal regions of TrxR-type FNRs, *Ct*FNR has a long, hydrophilic residue-rich C-terminal region, while that of *Bs*FNR is shorter (Fig. 1c). The differences in the C-terminal region may relate to the differences in catalysis between *Bs*FNR and *Ct*FNR with NADP⁺/NADPH.

To analyze the role of the C-terminal extension in *Ct*FNR during the redox reaction with NAD(P)⁺/NAD(P)H, we performed steady-state and pre-steady-state kinetic analyses of *Ct*FNR mutants with specific alterations designed to truncate the C-terminal region. The results obtained suggest that the C-terminal region controls the positioning of the nicotinamide ring portion of NADP⁺/H against the isoalloxazine ring portion of the FAD prosthetic group, leading to changes in the redox properties and reactivity toward NADP⁺/NADPH.

Materials and methods

Preparation of WT and mutant *CtFNRs*

Expression vectors for the truncation mutants of the C-terminal residues were prepared by replacement of the codons for Tyr326, Phe337 or Ser338 with a stop codon (TAA) by QuikChange site directed mutagenesis, utilizing the wild-type (WT) *CtFNR* expression vector (Muraki et al. 2008) as the template and with the following primers; 5'-CCACAGCCTCTCCTAAATCAAGCCGGGCGAG-3' and 5'-CTCGCCCGGCTTGATTTAGGAGAGGCTGTGG-3' for Δ Tyr326–Glu360, 5'-GAAAATTCGTAATGTCTAAAGCAGCGTCAAGATGGCCAAG-3' and 5'-CTTGCCATCTTGACGCTGCTTTAGACATTACGAATTTTC-3' for Δ Phe337–Glu360 or 5'-GAAAATTCGTAATGTCTTCTAAAGCGTCAAGATGGCCAAG-3' and 5'-CTTGCCATCTTGACGCTTTAGAAGACATTACGAATTTTC-3' for Δ Ser338–Glu360. The DNA sequence of the open reading frame of the mutated *CtFNR* gene was verified at the Institute for Genomic Research, Kanazawa University. The plasmids obtained were transformed into *E. coli* Tuner (DE3) pLacI cells (Novagen, Merck-Millipore, Merck KGaA, Germany). Expression and purification of mutated *CtFNRs* were performed using the same methods as for WT *CtFNR* (Seo et al. 2016b) except utilizing a Source 30Q anion exchange gel column (GE Healthcare UK Ltd., England) in place of a MonoQ column during the purification of Δ Phe337–Glu360 *CtFNR*. WT *CtFNR* was prepared as described in Seo et al. (2016b).

Steady-state enzyme assays

The NADPH diaphorase activity using potassium ferricyanide as the electron acceptor was measured in 20 mM 4-(2-hydroxyethyl)-1-piperazineethanesulfonic acid (HEPES)-NaOH buffer (pH 7.0) in the presence of 10 mM glucose-6-phosphate (G6P; Oriental Yeast Co., Ltd., Tokyo, Japan), 5 U/ml glucose-6-phosphate dehydrogenase (G6PDH, *Leuconostoc mesenteroides*; Biozyme Laboratories, Blaenavon, UK), 10 nM FNR and 2 mM potassium ferricyanide, together with 0–1 mM NADPH (Oriental Yeast Co., Ltd.) at 25°C under aerobic conditions, by monitoring the decrease in absorbance at 420 nm for 1 min using a double beam spectrophotometer (V-560, JASCO Co., Tokyo, Japan). The respective assay blank containing all of the assay reagents except FNR was subtracted for turnover rate estimation. Turnover rates are expressed as the number of NADPH molecules consumed by one homo-dimeric FNR. The Michaelis constant (K_M) and k_{cat} values were evaluated by nonlinear regression analysis using the Michaelis-Menten equation in Igor Pro software (ver. 6.3, WaveMetrics, Portland, OR, USA).

Stopped-flow spectrophotometry

Stopped-flow spectrophotometry was performed using a stopped-flow system with a photodiode array detector (Unisoku Co., Ltd., Osaka, Japan) in a glove box under a nitrogen atmosphere containing approximately 5% hydrogen as described in Seo et al. (2016a). The reaction was initiated by mixing equal volumes of solutions in single-mixing mode at 10°C. Transient spectra were recorded every 1 ms after mixing. The dead-time of the setup was estimated to be approximately 1 ms (Seo et al. 2016a). Concentrations of the *CtFNR* protomers and NADP⁺/NADPH/(4S-2H)-NADPD are provided as the final concentrations after mixing, unless otherwise noted.

Reduced *CtFNR* (*CtFNR*_{red}) was prepared with dithionite in the presence of methyl viologen followed by the removal of the latter by size-exclusion chromatography, as described previously (Seo et al. 2016b). The concentration of reduced *CtFNR* was estimated from the absorbance of the air-reoxidized form.

Data collection and basic arithmetic operations on the transient spectra were performed using Unispec (ver. 2.51, Unisoku Co., Ltd.) and Excel (ver. 15, Microsoft Corporation, Redmond, WA, USA) software. The transient absorptions at a single wavelength were fitted to exponential decay functions in Igor Pro software. The values of the absorbance at 457 nm (A_{457}) and A_{590} in Figs. 3b, 3d, 3f, 4b, 4d and 5b were estimated by subtracting A_{800} to compensate for the signal drift. Global analysis of the transient absorption data was performed with Olis GlobalWorks software (ver. 5.888.179, Olis Inc, USA). The selection of potential kinetic reaction models was made based on the weight values, and the spectral and kinetic eigenvectors of the components estimated by a singular value decomposition analysis. Model validity was assessed by kinetic and overall standard deviations of the fitting.

Miscellaneous methods

UV-visible absorption spectra were measured with a double beam spectrophotometer (V-560, JASCO) at 23 or 25°C. NADP⁺ titration was performed by the previously described method in 20 mM HEPES-NaOH buffer (pH 7.0) at 23 or 25°C (Seo et al. 2014). Difference spectra were obtained by subtracting the control spectrum recorded prior to the addition of NADP⁺ from the experimentally obtained spectra after correcting for volume changes. Dissociation constant (K_d) values were calculated according to Batie and Kamin (1984).

Thermal stabilities of the non-covalently bound FAD prosthetic group in the WT and mutated *CtFNR*s in oxidized form were measured by the previously described methods (Seo et al. 2015). *CtFNR* solution (~10 μM) in 20 mM HEPES-NaOH buffer (pH 7.0) was incubated at each temperature

over a range from 20 to 90°C for 5 min and then cooled on ice. After 20 min of centrifugation at 16,000 $\times g$, the supernatant was retained. Fluorescence intensity of the supernatant with excitation at 450 nm and emission at 525 nm was measured on a fluorescence spectrophotometer (F-2500, Hitachi, Japan). Data were fitted to a simple two-state transition model as described by John and Weeks (2000).

SDS-PAGE analysis was performed as described by Laemmli (1970). Protein bands on a 12% acrylamide gel were visualized with Coomassie Brilliant Blue R-250. Molecular weight marker (Precision Plus Protein Standard) was purchased from BioRad Lab. Inc., Japan.

Molecular masses of native forms of the enzymes were deduced by gel-permeation chromatography on a Superdex-200 10/300 column (GE Healthcare UK Ltd.) at a flow rate of 0.4 ml min^{-1} utilizing 20 mM tris(hydroxymethyl)aminomethane (Tris)-HCl buffer (pH 8.0) containing 200 mM NaCl as the eluent and molecular mass standards purchased from Sigma-Aldrich (Kit for Molecular Weights 12,000–200,000, MWGF200; St Louis, MO, USA).

Matrix assisted laser dye ionization-time of flight mass spectrometry (MALDI-TOF MS) analysis was performed utilizing an Ab Sciex 4800 Plus MALDI TOF/TOFTM analyzer (Sciex, Framingham, MA, USA) in the linear mode with sinapic acid as the matrix. Each data point was expressed as the mean value of the 40 times of integration of 50 shots at a laser intensity of 3000. Bovine serum albumin was used as a molecular mass standard.

Absorption coefficients for mutated *CtFNRs* were determined by the heat denaturation method as previously described (Aliverti et al. 1999; Seo et al. 2014). The extinction coefficient of 11.3 $\text{mM}^{-1} \text{cm}^{-1}$ at 450 nm was utilized for estimation of FAD concentration.

(4*S*-2H)-NADPD (the deuterated form of NADPH, referred to hereafter as *S*-NADPD) was prepared according to the method described in Seo et al. (2016a).

Protein and substrate concentrations were determined using the following extinction coefficients: WT *CtFNR* ($\epsilon_{466} = 10.3 \text{ mM}^{-1} \text{ cm}^{-1}$, Seo and Sakurai 2002), $\Delta\text{Tyr326-Glu360}$ *CtFNR* ($\epsilon_{457} = 10.3 \text{ mM}^{-1} \text{ cm}^{-1}$), $\Delta\text{Phe337-Glu360}$ *CtFNR* ($\epsilon_{457} = 10.6 \text{ mM}^{-1} \text{ cm}^{-1}$), $\Delta\text{Ser338-Glu360}$ *CtFNR* ($\epsilon_{458} = 10.3 \text{ mM}^{-1} \text{ cm}^{-1}$), potassium ferricyanide ($\epsilon_{420} = 1.02 \text{ mM}^{-1} \text{ cm}^{-1}$), and NADPH ($\epsilon_{340} = 6.2 \text{ mM}^{-1} \text{ cm}^{-1}$). NADP⁺ concentration was determined from the reduced form in the presence of excess G6P and G6PDH.

Results

Preparation and spectroscopic and molecular properties of WT and mutated *CtFNRs*

Three C-terminally truncated *CtFNRs*, Δ Tyr326–Glu360 *CtFNR*, Δ Phe337–Glu360 *CtFNR* and Δ Ser338–Glu360 *CtFNR* (hereafter designated Δ Y326 *CtFNR*, Δ F337 *CtFNR* and Δ S338 *CtFNR*, respectively) were purified to homogeneity (Fig. S1). The WT *CtFNR* polypeptide migrated with an apparent molecular mass of 42 kDa on SDS-PAGE (Fig. S1, Seo and Sakurai 2002). The apparent molecular masses of Δ Y326, Δ F337 and Δ S338 *CtFNRs* were approximately 38, 39 and 39 kDa based on SDS-PAGE, respectively (Fig. S1). MALDI-TOF MS analysis of WT *CtFNR* in the native form produced a major peak with a mass of 39.19 kDa (calculated mass, 39240 Da by sequence without FAD) (Fig. S2). Δ S338 showed a peak at 36.93 kDa (calculated mass, 36864 Da by sequence without FAD), and Δ Y326 at 35.33 kDa (calculated: 35420 Da by sequence without FAD) (Fig. S2). All the purified *CtFNRs* eluted as a single peak during gel-permeation chromatography. The deduced apparent molecular mass of WT *CtFNR* was approximately 91 kDa (Table 1), and the apparent molecular masses of Δ Y326, Δ F337 and Δ S338 *CtFNRs* were 68 kDa, 66kDa and 71 kDa, respectively (Table 1).

The UV-visible absorption spectra of Δ Y326, Δ F337, and Δ S338 *CtFNRs* exhibited FAD transition bands I and II in the near-UV to visible region with peaks centered around 456–458 nm and 378–381 nm, respectively (Fig. 2a). The absorption coefficients of WT and mutated *CtFNRs* at the λ_{\max} of the FAD transition band I (456–466 nm) exhibited similar values (10.3-10.6 mM⁻¹ cm⁻¹) (Fig. 2a, Table 1).

The thermal stabilities of bound FAD in the WT and the truncated *CtFNRs* were examined by measuring the flavin fluorescence emission of the retained supernatant after incubation and centrifugation (Fig. 2b). The temperatures providing 50% of the maximal difference in fluorescence intensity of Δ F337 and Δ S338 *CtFNRs* were estimated to be 69°C and 70°C, respectively, which were similar to that of WT (70°C). On the other hand, that of Δ Y326 *CtFNR* was estimated to be 62°C, which was 8°C lower than those of the WT *CtFNR*.

Steady-state assays with NADP⁺/NADPH

Addition of NADP⁺ to a solution of WT *CtFNR* induced blue-shifts and decreases in the flavin absorption bands, which produced troughs at approximately 514, 477, 445 and 404 nm in the difference spectrum (Fig. 2c). However, the addition of NADP⁺ to Δ Y326, Δ F337 and Δ S338 *CtFNR* solutions resulted in red-shifts and decreases in the bands, producing a peak at 504–505 nm and troughs at 477-478 and 450 nm in the difference spectra (Fig. 2c). Plots of the magnitude of spectral

changes, $\Delta A_{503-506}$ minus ΔA_{477} for $\Delta Y326$, $\Delta F337$ and $\Delta S338$ *CtFNR*s, and ΔA_{495} minus ΔA_{514} for WT *CtFNR* against NADP⁺ concentration yielded saturation curves (Fig. 2d). The K_d values for NADP⁺ for $\Delta Y326$, $\Delta F337$ and $\Delta S338$ *CtFNR*s were slightly higher than that for WT *CtFNR* (Table 1).

To evaluate the reactivity of the WT and truncated *CtFNR*s with NADPH, the turnover rate of diaphorase activity was measured using potassium ferricyanide as the electron acceptor (Table 1). On truncation of the C-terminal extension, the k_{cat} and K_M values for NADPH for the three mutants decreased slightly when compared to those for WT *CtFNR* (Table 1). As a result, the k_{cat}/K_M values of the truncation mutants were of the same order of magnitude as that of the WT *CtFNR*.

Pre-steady-state reaction of $\Delta Y326$ *CtFNR*_{ox} with NADPH/S-NADPD

The reaction of 9.3 μM $\Delta Y326$ *CtFNR*_{ox} with 100–500 μM NADPH was measured by stopped-flow spectrophotometry (Fig. 3a, b). Mixing $\Delta Y326$ *CtFNR*_{ox} with NADPH resulted in a rapid decrease in the flavin absorption band I (peak centered around 457 nm) within the dead-time of the instrument (~1 ms). The absorbance of this band decreased to an almost fully-reduced level by 1999 ms (Fig. 3a). The absorbance change at 457 nm contains four distinctive kinetic components designated as phase I, II, III and IV in order of the rate constants from fastest to slowest (Fig. 3b).

Phase I, observed as a rapid drop within the dead-time, was too rapid to trace in our stopped-flow system (>500 s⁻¹). The Δ absorbance of phase I was almost the same at the NADPH concentrations used (100–500 μM ; traces b–d in Fig. 3b). Mixing with *S*-NADPD in place of NADPH also resulted in a rapid drop with a similar Δ absorbance as that for NADPH (trace e in Fig. 3b).

After the rapid drop, A_{457} decreased gradually in the 1 to 1000 ms time period (Fig. 3b). The absorption change at 457 nm could be approximated by a three-step reaction model (red lines in Fig. 3b, Table 2). The observed rate constant (k_{obs}) of phase II (k_1 in Table 2), which appeared as a major decay component at 0–10 ms, became almost constant at NADPH concentrations above 200 μM with a value of ~ 200 s⁻¹. The amplitude of phase III (ΔA_2 in Table 2) increased with increasing NADPH concentration, and its k_{obs} (k_2 in Table 2) was nearly independent of the NADPH concentration used, with a value of ~ 30 s⁻¹. The k_{obs} of phase IV (k_3 in Table 2), observed as a slope after 200 ms, was estimated to be 3–3.5 s⁻¹ using the data in the time range 0 to 999 ms.

Upon mixing with 100 μM *S*-NADPD in place of NADPH, the absorption change at 457 nm after the rapid drop could be approximated by a two-step reaction model (trace e in Fig. 3b). The rate of phase II was estimated to be 16.2 ± 0.4 s⁻¹, and that of the slower phase was uncertain because the absorption change continued beyond the measurement time scale.

In the reaction with NADPH and *S*-NADPD, A_{590} in the charge transfer (CT) band region (Seo et al 2016a, b) rapidly increased within the instrument dead-time and reached its maximum intensity by 2

ms (Fig. 3a, inset of Fig.3b). Subsequently, the absorption intensity of this CT band decreased over 999 ms without a significant peak shift (Fig. 3a). Use of higher NADPH concentration (100–500 μM) did not significantly affect the maximum absorption intensity of the CT band (inset of Fig. 3b). The A_{590} can be approximated by a single-step reaction model (inset of Fig.3b). Obtained k_{obs} values were $27.4 \pm 0.8 \text{ s}^{-1}$ at 100 μM NADPH and $26.9 \pm 0.6 \text{ s}^{-1}$ at 500 μM NADPH.

To clarify any kinetic components induced by the use of excess NADPH, mixing with equimolar NADPH (25 μM) was performed as a reference (Fig. 3c, d). The observed absorption change at 457 nm after the rapid drop could be approximated by a two-step reaction model (red line in Fig. 3d, Table 2). The faster phase had a comparable rate constant (117 s^{-1}) to that of phase II with excess NADPH (100–500 μM), and the slower phase had a similar rate constant (3.1 s^{-1}) to that of phase IV in the excess NADPH experiments (Table 2)

Global analysis of the time-resolved absorption spectra implied that the reactions mixing with excess NADPH were approximated by a three-step sequential reaction model ($A \rightarrow B \rightarrow C \rightarrow D$ [fast/moderate/slow]) (inset of Fig.3a), and those with equimolar NADPH were approximated by a two-step sequential reaction model ($A \rightarrow B \rightarrow C$ [fast/slow]) (inset of Fig. 3c). The resulting rate constant for each reaction step (represented in the parentheses in Table 2) was comparable to that of the calculated value from the single wavelength analysis. The resulting spectrum of each of the kinetic components is shown in the insets of Fig. 3a, 3c.

Pre-steady-state reaction of $\Delta\text{Y326 CtFNR}_{\text{red}}$ with NADP^+

Mixing $\Delta\text{Y326 CtFNR}_{\text{red}}$ (10.6 μM) with NADP^+ resulted in a slow increase in the flavin absorption band I (Fig. 3e, f). The total absorption changes at near-equilibrium (i.e., at 1999 ms) exhibited a significant dependence on the NADP^+ concentration in the range of 100 to 500 μM (Fig. 3f). A_{457} in the 0 to 1999 ms time period could be approximated by a single-step reaction model (Fig. 3f). The k_{obs} values were estimated to be 6.05 ± 0.01 , 5.45 ± 0.01 and $4.61 \pm 0.01 \text{ s}^{-1}$ at 100, 200 and 500 μM NADP^+ , respectively. From ΔA_{457} at 3999 ms, the oxidation level of CtFNR was estimated to be approximately 40% at 100 μM NADP^+ (Fig. 3e).

In contrast to the reaction of $\Delta\text{Y326 CtFNR}_{\text{ox}}$ with NADPH (Fig. 3a), no significant absorption change was observed in the CT band region (550–800 nm) during the reaction in the NADP^+ concentration range of 100–500 μM (Fig. 3e).

The global analysis confirmed that the reactions mixing with NADP^+ were approximated by a single-step reaction model ($A \rightarrow B$) with a rate constant of $6.04 \pm 0.06 \text{ s}^{-1}$ at 100 μM NADP^+ (inset of Fig.3e).

Pre-steady-state reactions of $\Delta\text{S338 CtFNR}_{\text{ox}}$ with NADPH/S-NADPD

The reaction of 9.3 μM $\Delta\text{S338 CtFNR}_{\text{ox}}$ with NADPH resulted in a rapid decrease in the flavin absorption band I (peak centered around 457 nm) within the dead-time of the instrument (~ 1 ms), subsequently, the absorbance of this band decreased gradually to around 40% of that of $\Delta\text{S338 CtFNR}_{\text{ox}}$ at 3999 ms (Fig. 4a). The analyses of the absorbance change at 457 nm with NADPH and *S*-NADPD contained four distinctive kinetic components, designated as phase I, II, III and IV in order of the rate constants from fastest to slowest (Fig. 4b).

The Δ absorbance of the rapid absorption drop within the dead-time at 457 nm was similar at the NADPH concentration used (100–500 μM) (trace b-d in Fig. 4b). Although mixing with 100 μM *S*-NADPD in place of NADPH also resulted in a rapid drop within the dead time (trace e in Fig. 4b), its Δ absorbance was smaller than that with NADPH (trace b in the inset of Fig. 4b). After the drop, an additional small decay component appeared in the 0 to 5 ms time period (trace e in the inset of Fig. 4b). Corresponding to the results of mixing $\Delta\text{Y326 CtFNR}_{\text{ox}}$ with NADPH, the former *S*-NADPD-independent rapid drop is designated as phase I and the latter *S*-NADPD dependent decay is designated as phase II in the Discussion section.

After the rapid drop with NADPH, A_{457} decreased gradually in the 1 to 1000 ms time period (Fig. 4b). The absorption change with NADPH in this time period could be approximated by a two-step reaction model (red lines in Fig. 4b). The Δ absorbance of phase III, a major decay component in the 1 to 100 ms time period, increased with increasing NADPH concentration, and k_{obs} of this phase decreased with increasing NADPH concentration (ΔA_I and k_1 in Table 3). The absorption change at 457 nm upon mixing with 100 μM *S*-NADPD could be approximated by a three-step reaction model (trace e in Fig. 4b); k_{obs} of phase II was estimated to be $310 \pm 12 \text{ s}^{-1}$, and phase III was estimated to be $33.7 \pm 0.7 \text{ s}^{-1}$. The k_{obs} of phase IV (k_2 in Table 3), observed as a slope beyond 100 ms with both NADPH and *S*-NADPD, was uncertain, as this phase continued beyond the measurement time scale.

In the reaction of $\Delta\text{S338 CtFNR}_{\text{ox}}$ with NADPH and *S*-NADPD, the absorbance around 600 nm which corresponds to the formation of CTCs (Seo et al 2016a, b), rapidly increased within the dead-time and reached its maximal intensity by 5 ms (Fig. 4a). Subsequently, the intensity of this absorption band decreased slightly with time, without a significant peak shift by 3999 ms (Fig. 4a). The NADPH concentration used (100–500 μM) hardly affected the maximum absorption intensity of the CT band.

Global analysis of the transient absorption indicated that the reaction mixing with excess NADPH was approximated by a three-step sequential reaction model ($\text{A} \rightarrow \text{B} \rightarrow \text{C} \rightarrow \text{D}$ [fast/moderate/slow]) with similar rate constants to the single wavelength analysis except for the presence of an additional faster phase (represented in the parentheses in Table 3). The resulting spectrum of each kinetic component is shown in the inset of Fig. 4a.

Pre-steady-state reaction of Δ S338 *CtFNR*_{red} with NADP⁺

Mixing Δ S338 *CtFNR*_{red} (11.7 μ M) with NADP⁺ resulted in a slow increase in the flavin absorption band I (Fig. 4c, d). The total absorption change at near-equilibrium (i.e., at 1999 ms) showed a significant dependence on the NADP⁺ concentration in the range of 100–500 μ M (Fig. 4d). In the 0 to 1999 ms time period, A_{457} could be approximated by a two-step reaction model (red lines in Fig. 4d). The k_{obs} values of the faster phase were estimated to be 7.70 ± 0.02 , 7.04 ± 0.018 and 5.94 ± 0.02 at 100, 200 and 500 μ M NADP⁺, respectively. As the absorption change continued beyond the measurement timescale, the k_{obs} value of the slower phase was uncertain ($<4 \text{ s}^{-1}$). From ΔA_{457} at 3999 ms, the oxidation level of Δ S338 *CtFNR* was estimated to be approximately 60% at 100 μ M NADP⁺ (Fig. 4c). No significant absorption change was observed in the CT band region (550–800 nm) during the reaction, in the 100–500 μ M NADP⁺ concentration range (Fig. 4c). Global analysis implied that the reaction mixing with NADP⁺ was approximated by a two-step sequential reaction model (A→B→C [fast/slow]) with rate constants of 7.70 ± 0.19 and 1.14 ± 0.09 for the first and second reaction steps, respectively, at 100 μ M NADP⁺. The spectrum of each of the kinetic components is shown in the inset of Fig.4c.

Pre-steady-state reactions of Δ F337 *CtFNR*_{ox} with NADPH/S-NADPD

To determine if the difference in the pre-steady state kinetics of the NADPH/S-NADPD oxidation reaction between Δ Y326 *CtFNR* and Δ S338 *CtFNR* corresponds to the absence of Phe337, we prepared Δ F337 *CtFNR* and evaluated the effect of this mutation on the NADPH/S-NADPD oxidation reactions by stopped-flow spectrophotometry (Fig. 5a, b).

The reaction of 9.0 μ M Δ F337 *CtFNR*_{ox} with NADPH resulted in a rapid decrease in the flavin absorption band I within the dead-time and then the absorbance of this band decreased gradually (Fig. 5a). The absorption changes at 457 nm upon mixing with NADPH and S-NADPD contained four distinctive kinetic components, designated as phase I, II, III and IV in order of the rate constants from fastest to slowest (Fig. 5b).

Although the Δ absorbance of the rapid absorption drop at 457 nm was similar at all of the NADPH concentrations used (100–500 μ M) (trace b-d in Fig. 5b), the Δ absorbance of mixing with 100 μ M S-NADPD (trace e in the inset of Fig. 5b) was smaller than that of mixing with 100 μ M NADPH (trace b in the inset of Fig. 5b). After the drop, an additional small decay component appeared in the 0 to 5 ms time period (trace e in the inset of Fig. 5b) just as with Δ S338 *CtFNR* (Fig. 4b). After the rapid drop, A_{457} decreased gradually in the 2 to 1000 ms time period for NADPH (or in the 5 to 1000 ms time period for S-NADPD) (Fig. 5b). In the reaction with NADPH, the absorption change in this time period could be approximated by a two-step reaction model (red lines in Fig. 5b). With increasing

NADPH concentration, the Δ absorbance of phase III, a major decay component observed in the 2 to 100 ms time period increased, and k_{obs} of this phase decreased (ΔA_1 and k_1 in Table 4). The absorption change upon mixing with 100 μM *S*-NADPD could be approximated by a three-step reaction model (trace e in Fig. 5b). The k_{obs} values of phases II and III were estimated to be $239 \pm 6 \text{ s}^{-1}$ and $14.7 \pm 0.2 \text{ s}^{-1}$, respectively (trace e in Fig. 5b). k_{obs} of phase IV (k_2 in Table 4), observed as a slope beyond 100 ms with both NADPH and *S*-NADPD, was uncertain, as this phase continued beyond the measurement time scale.

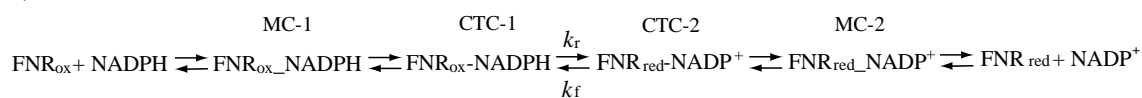
In the reaction of $\Delta\text{F337 CtFNR}_{\text{ox}}$ with NADPH and *S*-NADPD, the absorbance around 600 nm which corresponds to the formation of CTCs (Seo et al 2016a, b) rapidly increased within the dead-time and reached its maximum intensity by 5 ms (Fig. 5a). Subsequently, the intensity of this absorption band decreased slightly with time, without a significant peak shift by 3999 ms (Fig. 5a).

Global analysis of the transient spectra indicated that the reactions with NADPH were approximated by a two-step sequential reaction model ($A \rightarrow B \rightarrow C$ (fast/slow)) with similar rate constants to those of the single wavelength analyses (Table 4). The resulting spectrum for each kinetic component is shown in the inset of Fig. 5a.

Discussion

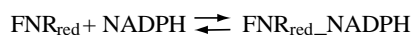
In this study, $\Delta Y326$, $\Delta F337$ and $\Delta S338$ C-terminal truncation variants of *CtFNR* showed apparent molecular masses corresponding to a homodimeric form, as was also observed for WT *CtFNR* (Table 1). Compared with the flavin absorption bands of the WT *CtFNR*, those of the truncation mutants shifted toward shorter wavelength (Fig. 2a), indicating that the truncations perturbed the environment of the FAD isoalloxazine ring. The truncation of the corresponding region in *BsFNR* and replacement of Phe337 in *CtFNR* also resulted in blue-shifts of the flavin absorption bands (Muraki et al. 2010; Seo et al. 2014). The difference spectra of the truncation mutants induced by the addition of NADP⁺ were similar to that of the Phe337Ser mutant rather than those of Phe337His and Phe337Tyr mutants (Muraki et al. 2010). These indicate a loss of hydrogen bonding, a change in the polarity and/or a loss of the dipole field of the C-terminal helix could cause the observed spectral changes (Yagi et al. 1980; Heelis 1982). Although the truncations induce substantial changes in the environment of the FAD isoalloxazine ring, the thermal stability of the bound FAD prosthetic group was not drastically modulated (Fig. 2b). In steady-state reactions with NADP⁺ and NADPH, K_d , K_M and k_{cat} values of the truncated *CtFNRs* were similar (70–180% of those of WT *CtFNR*) (Table 1). Pre-steady-state kinetics, however, indicated that the truncation mutations significantly altered the kinetics and equilibria of the reactions with NADP⁺/NADPH.

In the NADPH oxidation reaction with $\Delta S338$ and $\Delta F337$ *CtFNR*_{S_{ox}}, the CT absorption band centered around 600 nm appeared within the experimental dead-time and reached its maximal intensity by 5 ms. The NADPH concentration used did not significantly affect the maximal intensity. These results are consistent with the rapid formation of Michaelis complex 1 (FNR_{ox}_NADPH, MC-1) before the formation of CTC-1 (Scheme 1; Lennon and Williams Jr. 1997, Tejero et al. 2007; Seo et al. 2016a, b).



Scheme 1

When *S*-NADPD was used in place of NADPH, a small decay component was observed from 0 to 5 ms (phase II) (trace e in Fig. 4b, 5b), indicating that phase II was affected by the deuterium substitution. Because k_{obs} decreased and the Δ absorbance increased with increasing NADPH concentration, phase III corresponds to the formation of the FNR_{red}-NADPH complex (Scheme 2) (Seo et al. 2016a, b).



Scheme 2

These results suggest that the hydride transfer process in the reaction of $\Delta F337$ and $\Delta S338$ *CtFNR*_{S_{ox}} with NADPH is very fast, as is the case for WT *CtFNR* (Daff 2004; Seo et al. 2016b).

In contrast, NADPH oxidation by $\Delta Y326$ *CtFNR*_{ox} gave rise to a slow absorption change after

the initial rapid drop in the flavin absorption band I (Fig. 3a, b). In phase I of $\Delta Y326$ *CtFNR*_{ox}, mixing with NADPH and *S*-NADPD provided a similar Δ absorbance (Fig. 3b). In this period, the equilibria between *FNR*_{ox} and CTC-1 (Scheme 1) almost reached completion because the absorbance of the CT band nearly reached its maximum (inset of Fig.3b). Next, k_{obs} values of phase II (k_1 in Table 2) were almost constant between 200-500 μM NADPH (Table 2) and became markedly slower upon deuterium substitution (15 s^{-1} vs. $\sim 200\text{ s}^{-1}$, kinetic isotope effect value ≈ 13) (Fig. 3b trace b–e). Also, the Δ absorbance of phase II was almost same between 200-500 μM NADPH (ΔA_1 in Table 2). Third, the amplitude of phase III in NADPH oxidation by $\Delta Y326$ *CtFNR*_{ox} increased with increasing NADPH concentration (ΔA_2 in Table 2). Upon mixing with equimolar NADPH, phase III was absent (Fig. 3d; Table 2). Such a NADPH concentration dependence of phase III after formation of MC-1 in the system represented in Scheme 1 can be explained by the formation of the *CtFNR*_{red}-NADPH complex (Scheme 2) (Batie and Kamin 1986, Seo et al. 2016a,b). These results indicate that the k_{obs} of phase II would correspond to the hydride transfer rate, $k_f + k_r$ (Scheme 1) in the case of $\Delta Y326$ *CtFNR*. Accordingly, $k_f + k_r$ can be estimated to be $\sim 200\text{ s}^{-1}$ from k_1 in Table 2 (Daff 2004; Seo et al. 2016a). The smaller $k_f + k_r$ value of $\Delta Y326$ *CtFNR* compared with those of WT, $\Delta F337$ and $\Delta S338$ *CtFNR*s ($>500\text{ s}^{-1}$) suggests that the residues Tyr326–Val336 contribute to an efficient hydride transfer between *NADP*⁺/*NADPH* and the FAD prosthetic group. It should be noted that although the rate of hydride transfer was significantly decreased in $\Delta Y326$ *CtFNR*, the value is still larger than the maximal velocity of the steady-state reaction assay ($\sim 400\text{ s}^{-1}/e^-$ at 10°C (Table 2) vs. $213\text{ s}^{-1}/e^-$ at 25°C (Table 1)), which may be the reason for the slight changes in the steady-state reaction parameters (Table I).

On our measurement timescale, phase IV seems unique to the reaction of $\Delta Y326$ *CtFNR*_{ox} with NADPH. Although the k_r/k_f ratio (Scheme 1) of $\Delta Y326$ *CtFNR* from the equilibrium of phase II (3:7, from $\Delta A_1/(\Delta A_2 + \Delta A_3)$ at 100 μM NADPH [Table 2]) was comparable to that of WT *CtFNR* (3:7, Seo et al. 2016b), the presence of phase IV drastically increased the amount of $\Delta Y326$ *CtFNR*_{red} at equilibrium with *NADP*⁺/*NADPH* compared to WT, $\Delta F337$ and $\Delta S338$ *CtFNR*s (Fig. 3a, 4a, 5a, Seo et al. 2016b). Based on the transient spectroscopic data and results of the global analyses, we could not assign a reaction step that would corresponded to phase IV. A comparison of the spectra of component B with those of component C and D in the inset of Fig. 3a proves decreases in the absorbance of both the flavin band I and the CT band region. It is likely that the equilibria in Scheme 1 and 2 changed in this phase, and the formation of uncertain species did not provide a substantial unique spectral feature distinctive from other *CtFNR*_{red}-related species.

Previous pre-steady state kinetic studies of the reactions of WT *BsFNR* and WT *CtFNR* with *NADP*⁺/*NADPH* confirmed that the reaction involves formation of both CTC-1 (*FNR*_{ox}-*NADPH*) and CTC-2 (*FNR*_{red}-*NADP*⁺), with the appearance of CT absorption bands centered at approximately 600 nm (Blankenhorn 1975; Seo et al. 2016a, b). In this work, $\Delta F337$ and $\Delta S338$ *CtFNR*s also exhibited a CT absorption band centered at around 600 nm during their reduction by NADPH (Fig. 4a, 5a),

indicating formation of CTC-1 and CTC-2 (Seo et al 2016a, b). For $\Delta Y326$ *CtFNR*, A_{590} only contained one kinetic component with a corresponding rate constant ($\sim 27 \text{ s}^{-1}$) (inset of Fig.3b) similar to that of phase III at A_{457} ($\sim 30 \text{ s}^{-1}$, k_2 in Table 2), and global analysis provided the spectra of kinetic component B, which had a similar intensity for the CT band compared to that of kinetic component A (in the inset of Fig. 3a). Thus, CTC-2 of $\Delta Y326$ in the NADPH oxidation reaction also possesses a CT absorption band.

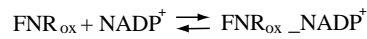
For phase IV, the global analysis indicated that a substantial amount of CTC-1 and CTC-2 remained at equilibrium in $\Delta F337$ and $\Delta S338$ *CtFNR*s (components C and D in the insets of Fig. 4a, 5a), whereas CTC-1 and CTC-2 are almost omitted in $\Delta Y326$ *CtFNR* (component D in the inset of Fig.3a). As the redox potential of the free FAD molecule is higher than that of the $\text{NADP}^+/\text{NADPH}$ couple, interactions of FAD with the protein peptide chains are indispensable for regulating redox properties for catalysis. As *CtFNR* undertakes NADP^+ reduction rather than NADPH oxidation under physiological conditions, such regulations might result in a drastic change of the redox properties of the FAD prosthetic group. Our results indicate that the C-terminal region of *CtFNR* participates in the stabilization of CTCs, thereby regulating the redox properties. It should be noted that the C-terminal region of one protomer covers the *re*-face of the other protomer in the TrxR-type FNR, which would explain the requirement for the formation of a homodimer as the catalytic unit. Although kinetic analyses in this work can be performed without consideration of the differences in kinetic behavior for each protomer, we cannot exclude the possibility that phase IV is related to a decreased contact between the protomers due to the truncation.

In reports on flavoproteins of the transhydrogenase family with the two-nucleotide binding domain architecture, the role of the *re*-face aromatic residue in hydride transfer has often been investigated. In the crystal structure of human GR with NADP^+ , the *re*-face Tyr197 residue stacking over the nicotinamide ring portion of NADP^+ compresses the nicotinamide ring portion of NADP^+ toward the isoalloxazine ring portion of the FAD, resulting in a closer contact between N5 of the isoalloxazine ring portion of FAD and C4 of the nicotinamide ring portion of NADP^+ , thereby enhancing the hydride transfer (Berkholz et al. 2008). Based on molecular dynamics and quantum mechanics/molecular mechanics simulation of plant-type *Anabaena* FNR, it has been proposed that the presence of the C-terminal residue Tyr303 on the *re*-face of the isoalloxazine ring portion of the FAD prosthetic group suppresses the interaction between the isoalloxazine ring portion of the FAD hydroquinone anion and the nicotinamide ring portion of NADP^+ , which contributes to an efficient hydride transfer toward NADP^+ (i.e. NADP^+ reduction) (Lans et al. 2012; Mulo and Medina 2017).

In the case of the TrxR-type FNR, a motion of the NADPH-binding domain toward FAD-binding domain may allow the positioning of the nicotinamide ring portion of $\text{NADP}^+/\text{NADPH}$ close to the isoalloxazine ring portion of the FAD prosthetic group for hydride transfer (Waksman et al. 1994; Komori et al. 2010). Our result suggests that the C-terminal extension of *CtFNR* interacts with the

NADPH binding domain thereby stabilizing the conformation of the CTCs. In this process, Phe337 plays a role differently than in the other enzymes. In previous works, replacements of Phe337 also did not significantly affect the steady-state reaction parameters (Muraki et al. 2010). However, it should be noted that any mechanism for the enhancement of hydride transfer involving the C-terminal region of *CtFNR* might be complicated by the cooperation of other structural factors such as ternary complex formation with Fd (Batie and Kamin 1984). The dynamics of the C-terminal region of *CtFNR* should be investigated for further understanding of the catalytic details of this protein.

During NADP⁺ reduction by the WT, $\Delta Y326$ and $\Delta S338$ *CtFNR*_{S_{red}}, the k_{obs} of the faster component of A_{457} decreased with increasing NADP⁺ concentration (Fig. 3f, 4d). Total absorption changes at 457 nm at 1999 ms demonstrated a significant dependence on NADP⁺ concentration in the range of 100 to 500 μM (Fig. 3f, 4d). These results indicate that the formation of an FNR_{ox}-NADP⁺ complex occurred (Scheme 3), in addition to the reactions in Scheme 1 (Seo et al. 2016a, b). In WT



Scheme 3

and both mutated *CtFNR*s, the k_{obs} of the fastest component of the change in A_{457} give a similar rate constant of 3–7 s⁻¹. During NADP⁺ reduction by WT, $\Delta Y326$ and $\Delta S338$ *CtFNR*_{S_{red}}, we did not observe a CT band, which makes the determination of the rate-limiting step difficult (Seo et al. 2016b). However, we can conclude that the C-terminal region did not significantly affect the rate-limiting process during NADP⁺ reduction by *CtFNR*_{red} in the absence of Fd.

References

- Aliverti A, Curti B, Vanoni MA (1999) Identifying and quantitating FAD and FMN in simple and in iron-sulfur-containing flavoprotein. In: Chapman SK, Reid GA (eds) Flavoprotein protocols. Vol. 131. Methods in Molecular Biology. Humana Press, Totowa, New Jersey, USA, pp 9-23
- Aliverti A, Pandini V, Pennati A, de Rosa M, Zanetti G (2008) Structural and functional diversity of ferredoxin-NADP⁺ reductases. *Arch Biochem Biophys* 474:283-291
- Batie CJ, Kamin H (1984) Ferredoxin:NADP⁺ oxidoreductase. Equilibria in binary and ternary complexes with NADP⁺ and ferredoxin. *J Biol Chem* 259:8832-8839
- Batie CJ, Kamin H (1986) Association of ferredoxin-NADP⁺ reductase with NADP(H) specificity and oxidation-reduction properties. *J Biol Chem* 261:11214-11223
- Berkholz DS, Faber HR, Savvides SN, Karplus PA (2008) Catalytic cycle of human glutathione reductase near 1 Å resolution. *J Mol Biol* 382:371-384
- Blankenhorn G (1975) Flavin nicotinamide biscoenzymes: models for the interaction between NADH (NADPH) and flavin in flavoenzymes. Reaction rates and physicochemical properties of intermediate species. *Eur J Biochem* 50:351-356
- Bortolotti A, Sánchez-Azqueta A, Maya CM, Velázquez-Campoy A, Hermoso, JA, Medina M., Cortez N (2014) The C-terminal extension of bacterial flavodoxin-reductases: Involvement in the hydride transfer mechanism from the coenzyme. *Biochim Biophys Acta* 1837:33-43
- Ceccarelli EA, Arakaki AK, Cortez N, Carrillo N (2004) Functional plasticity and catalytic efficiency in plant and bacterial ferredoxin-NADP(H) reductases. *Biochim Biophys Acta* 1698:155-165
- Correll CC, Ludwig ML, Bruns CM, Karplus PA (1993) Structural prototypes for an extended family of flavoprotein reductases: comparison of phthalate dioxygenase reductase with ferredoxin reductase and ferredoxin. *Prot Sci* 2:2112-2133
- Daff S (2004) An appraisal of multiple NADPH binding-site models proposed for cytochrome P450 reductase, NO synthase, and related diflavin reductase systems. *Biochemistry* 43:3929-3932

- Dym O, Eisenberg D (2001) Sequence-structure analysis of FAD-containing proteins. *Prot Sci* 10:1712-1728
- Heelis PF (1982) The photophysical and photochemical properties of flavins (isoalloxazines). *Chemical Society Reviews* 11:15-39
- John DM, Weeks KM (2000) van't Hoff enthalpies without baselines. *Prot Sci* 9: 1416-1419
- Karplus PA, Faber HR (2004) Structural aspects of plant ferredoxin: NADP⁺ oxidoreductases. *Photosyn Res* 81:303-315
- Komori H, Seo D, Sakurai T, Higuchi Y (2010) Crystal structure analysis of *Bacillus subtilis* ferredoxin-NADP⁺ oxidoreductase and the structural basis for its substrate selectivity. *Prot Sci* 19:2279-2290
- Lans I, Peregrina JR, Medina M, Garcia-Viloca M, González-Lafont À, Lluch JM (2010) Mechanism of the hydride transfer between anabaena Tyr303Ser FNR_{rd}/FNR_{ox} and NADP⁺/H. A combined pre-steady-state Kinetic/Ensemble-averaged transition-state theory with multidimensional tunneling study. *J Phys Chem B* 114:3368-3379
- Lans I, Medina M, Rosta E, Hummer G, Garcia-Viloca M, Lluch JM, González-Lafont A (2012) Theoretical study of the mechanism of the hydride transfer between ferredoxin-NADP⁺ reductase and NADP⁺: The role of Tyr303. *J Am Chem Soc* 134:20544-20553
- Laemmli UK (1970) Cleavage of structural proteins during the assembly of the head of bacteriophage T4. *Nature* 227:680-685
- Lennon BW, Williams Jr CH (1997) Reductive half-reaction of thioredoxin reductase from *Escherichia coli*. *Biochemistry* 36:9464-9477
- Medina M, Gómez-Moreno C (2004) Interaction of ferredoxin-NADP⁺ reductase with its substrates: optimal interaction for efficient electron transfer. *Photosyn Res* 79:113-131
- Mulo P, Medina M (2017) Interaction and electron transfer between ferredoxin–NADP⁺ oxidoreductase and its partners: structural, functional, and physiological implications. *Photosyn Res* (in press) doi:10.1007/s11120-017-0372-0.

Muraki N, Seo D, Shiba T, Sakurai T, Kurisu G (2008) Crystallization and preliminary X-ray studies of ferredoxin-NAD(P)⁺ reductase from *Chlorobium tepidum*. *Acta Crystallogr Sec F: Struc Biol Cryst Com* 64:186-189

Muraki N, Seo D, Shiba T, Sakurai T, Kurisu G (2010) Asymmetric dimeric structure of ferredoxin-NAD(P)⁺ oxidoreductase from the green sulfur bacterium *Chlorobaculum tepidum*: implications for binding ferredoxin and NADP⁺. *J Mol Biol* 401:403-414

Nogués I, Tejero J, Hurley JK, Paladini D, Frago S, Tollin G, Mayhew SG, Gómez-Moreno C, Ceccarelli EA, Carrillo N, Medina M (2004) Role of the C-terminal tyrosine of ferredoxin-nicotinamide adenine dinucleotide phosphate reductase in the electron transfer processes with its protein partners ferredoxin and flavodoxin. *Biochemistry* 43:6127-6137

Peregrina JR, Sánchez-Azqueta A, Herguedas B, Martínez-Júlvez M, Medina M (2010) Role of specific residues in coenzyme binding, charge-transfer complex formation, and catalysis in *Anabaena* ferredoxin NADP⁺-reductase. *Biochim Biophys Acta* 1797:1638-1646

Piubelli L, Aliverti A, Arakaki AK, Carrillo N, Ceccarelli EA, Karplus PA, Zanetti G (2000) Competition between C-terminal tyrosine and nicotinamide modulates pyridine nucleotide affinity and specificity in plant ferredoxin-NADP⁺ reductase. *J Biol Chem* 275:10472-10476

Seo D, Sakurai H (2002) Purification and characterization of ferredoxin-NAD(P)⁺ reductase from the green sulfur bacterium *Chlorobium tepidum*. *Biochim Biophys Acta* 1597: 123-132

Seo D, Kamino K, Inoue K, Sakurai H (2004) Purification and characterization of ferredoxin-NADP⁺ reductase encoded by *Bacillus subtilis* *yumC*. *Arch Microbiol* 182:80-89

Seo D, Asano T, Komori H, Sakurai T (2014) Role of the C-terminal extension stacked on the *re*-face of the isoalloxazine ring moiety of the flavin adenine dinucleotide prosthetic group in ferredoxin-NADP(+) oxidoreductase from *Bacillus subtilis*. *Plant Physiol Biochem* 81:143-148

Seo D, Naito H, Nishimura E, Sakurai T (2015) Replacement of Tyr50 stacked on the *si*-face of the isoalloxazine ring of the flavin adenine dinucleotide prosthetic group modulates *Bacillus subtilis* ferredoxin-NADP⁺ oxidoreductase activity toward NADPH. *Photosynth Res.* 125:321-328

Seo D, Soeta T, Sakurai H, Sétif P, Sakurai T (2016a) Pre-steady-state kinetic studies of redox reactions catalysed by *Bacillus subtilis* ferredoxin-NADP⁺ oxidoreductase with NADP⁺/NADPH and ferredoxin. *Biochim Biophys Acta* 1857:678-687

Seo, D, Kitashima M, Sakurai T, Inoue K (2016b) Kinetics of NADP⁺/NADPH reduction–oxidation catalyzed by the ferredoxin-NAD(P)⁺ reductase from the green sulfur bacterium *Chlorobaculum tepidum*. *Photosyn Res* 130:479-489

Tejero J, Pérez-Dorado I, Maya C, Martínez-Júlvez, M, Sanz-Aparicio J, Gómez-Moreno C, Hermoso JA, Medina M (2005) C-terminal tyrosine of ferredoxin-NADP⁺ reductase in hydride transfer processes with NAD(P)⁺/H. *Biochemistry* 44:13477-13490

Tejero J, Peregrina JR, Martínez-Júlvez M, Gutiérrez A, Gómez-Moreno C, Scrutton NS, Medina M (2007) Catalytic mechanism of hydride transfer between NADP⁺/H and ferredoxin-NADP⁺ reductase from *Anabaena* PCC 7119. *Arch Biochem Biophys* 459:79-90

Waksman G, Krishna TS, Williams Jr CH, Kuriyan J (1994) Crystal structure of *Escherichia coli* thioredoxin reductase refined at 2 Å resolution. Implications for a large conformational change during catalysis. *J Mol Biol* 236:800-816

Yagi K, Ohishi N, Nishimoto K, Choi JD, Song PS (1980) Effect of hydrogen bonding on electronic spectra and reactivity of flavins. *Biochemistry* 19:1553-1557

Figure legend

Fig. 1 (a, b) Close-up view around the isoalloxazine ring moiety of the FAD prosthetic group in the crystal structure of *Ct*FNR (PDB code: 3AB1). Main chains of subunits A and B are colored in magenta and aquamarine, respectively. Main chain of the residues 309-348 in subunit B are colored in blue. The side chains of Tyr57 in subunit A, Tyr326 and Phe337 in subunit B are colored in red and depicted as a stick model. The figure was prepared with Discovery Studio 4.0 Visualizer (Accelrys Inc., USA). (c) Partially aligned amino acid sequences of the C-terminal residues in TrxR-type FNRs and *Ec*TrxR. The number of the initial amino acid residue in each line is indicated at left side. The position of the residue stacked on the *re*-face of the isoalloxazine ring moiety is indicated by an arrow in the upper line. The positions of the 6th and 7th helices assigned in the crystal structure of *Ct*FNR (Muraki et al. 2010) and in *Ec*TrxR (Waksman et al. 1994) are indicated by the waves in the upper and bottom lines, respectively. The positions of C-termini of $\Delta Y326$, $\Delta F337$ and $\Delta S338$ *Ct*FNRs are indicated by arrows. bsu:YumC: *Bacillus subtilis subsp. subtilis* str. 168 FNR, rpa:RPA3954: *Rhodospseudomonas palustris* CGA009 FNR, cte:*Ct*FNR: *Chlorobaculum tepidum* FNR, eco:TrxR: *Escherichia coli* K12 TrxR.

Fig. 2 (a) near UV-visible absorption spectra of WT (black broken line), $\Delta Y326$ (red continuous line), $\Delta F337$ (green continuous line) and $\Delta S338$ (blue continuous line) *Ct*FNRs in the air-oxidized form. The spectra of approximately 10 μM *Ct*FNRs in 20 mM HEPES-NaOH buffer (pH 7.0) were measured at 23 or 25°C. Absorption coefficient of *Ct*FNR was estimated based on the FAD concentration as described in the Materials and methods section. (b) Thermal stability profiles of air oxidized WT (black circle), $\Delta Y326$ (red square), $\Delta F337$ (green diamond) and $\Delta S338$ (blue triangle) *Ct*FNRs. The supernatant (9-10 μM *Ct*FNR) after incubation at indicated temperature for 5 min followed by centrifugation was retained. Fluorescence intensity of the diluted supernatant (4-5 μM FAD) with excitation at 450 nm and emission at 525 nm was measured. The fluorescence intensities are normalized by subtracting the intensity at 20°C and dividing by the difference intensity between 20°C and 90°C. Each data is average of two or three measurements. (c) Difference spectra of WT (black broken line), $\Delta Y326$ (red continuous line), $\Delta F337$ (green continuous line) and $\Delta S338$ (blue continuous line) *Ct*FNRs induced by the addition of 1 mM NADP⁺. Measurements were performed at 23 or 25°C in 20 mM HEPES-NaOH buffer (pH 7.0). (d) Relationship between the magnitude of spectral change and NADP⁺ concentration. Spectral change on the difference spectra of WT *Ct*FNR (black circle): $\Delta\epsilon_{495} - \Delta\epsilon_{514}$, $\Delta Y326$ *Ct*FNR (red square): $\Delta\epsilon_{505} - \Delta\epsilon_{477}$, $\Delta F337$ *Ct*FNR (green diamond): $\Delta\epsilon_{503} - \Delta\epsilon_{477}$ and $\Delta S338$ *Ct*FNR (blue triangle): $\Delta\epsilon_{506} - \Delta\epsilon_{477}$ are plotted against NADP⁺ concentration. Each NADP⁺ solutions were added to the cuvettes containing ~10 μM *Ct*FNR solutions in 20 mM HEPES-NaOH buffer (pH 7.0) for the sample cell and 20 mM HEPES-NaOH buffer (pH 7.0) only for the reference cell.

Fig. 3. (a) Transient spectra induced by mixing 9.3 μM $\Delta\text{Y326 } Ct\text{FNR}_{\text{ox}}$ with 100 μM NADPH. The reaction was performed in 20 mM HEPES-NaOH buffer (pH 7.0) at 10°C. The spectra at 1 ms, 9ms, 99 ms and 999 ms are shown as thin continuous lines. The spectra shown by thin dotted lines from the top to the bottom at 450 nm correspond to those at 2, 19, 49, 199 499, and 1999 ms, respectively. The spectrum of $\Delta\text{Y326 } Ct\text{FNR}_{\text{ox}}$ in the absence of NADPH is shown as a thick continuous line. The arrows indicate the directions of the absorbance changes at the respective wavelengths. The dashed parts of the arrows indicate change that occurred within the first data acquisition period (1 ms). The inset shows the spectrum of each kinetic component resulting from global analysis of the transient spectra with three-step sequential reaction model ($A \rightarrow B \rightarrow C \rightarrow D$ [fast/moderate/slow]). (b) The time course of A_{457} after mixing $\Delta\text{Y326 } Ct\text{FNR}_{\text{ox}}$ with NADPH and S -NADPD. The measurement conditions were the same as those in Fig. 3a except the NADPH concentrations of 0 μM (trace a), 100 μM (trace b), 200 μM (trace c) and 500 μM (trace d). The time course of A_{457} after mixing $\Delta\text{Y326 } Ct\text{FNR}_{\text{ox}}$ with 100 μM S -NADPD is shown with normalization of $Ct\text{FNR}$ concentration (trace e). The data are an average of four to five measurements. The red lines indicate fitted curves with two (trace e) or three (trace b-d) exponential components. The residuals are indicated as black lines (NADPH) and a red line (S -NADPD) in the lower figure panel. The inset shows time course of A_{590} after mixing $\Delta\text{Y326 } Ct\text{FNR}_{\text{ox}}$ with 100 μM (trace b) and 500 μM (trace d) NADPH. Red lines indicate fitted curves with one exponential component. The residuals are shown as black lines (trace f). (c) Transient spectra induced by mixing 25 μM $\Delta\text{Y326 } Ct\text{FNR}_{\text{ox}}$ with 25 μM NADPH. The reaction was performed in 20 mM HEPES-NaOH buffer (pH 7.0) at 10°C. The spectra at 9, 99 and 999 ms are shown as thin continuous lines. The spectra shown by thin dotted lines from the top to the bottom at 450 nm correspond to those at 4, 19, 49, 199 499, and 1999 ms, respectively. The spectrum of $\Delta\text{Y326 } Ct\text{FNR}_{\text{ox}}$ is shown as a thick continuous line. The arrows indicate the directions of the absorbance changes at the respective wavelengths. The dashed parts of the arrows indicate changes that occurred within the first data acquisition period (1 ms). The inset shows the spectrum of each kinetic component resulting from global analysis of the transient spectra with two-step sequential reaction model ($A \rightarrow B \rightarrow C$ [fast/slow]). (d) The time course of A_{457} after mixing 25 μM $\Delta\text{Y326 } Ct\text{FNR}_{\text{ox}}$ with 25 μM NADPH. The measurement conditions were the same as those in Fig. 3c. The data are an average of four measurements. The red line represents a fitted curve with two exponential components. The residual is indicated in the lower figure panel. (e) Transient spectra induced by mixing 10.6 μM $\Delta\text{Y326 } Ct\text{FNR}_{\text{red}}$ with 100 μM NADP^+ . The reaction was performed in 20 mM HEPES-NaOH buffer (pH 7.0) at 10°C. The spectra at 1 ms, 99 ms and 999 ms are shown as thin continuous lines. The spectra shown by thin dotted lines from the bottom to the top at 450 nm correspond to those at 19, 49, 199, 499 and 1999 ms. The spectrum of $\Delta\text{Y326 } Ct\text{FNR}_{\text{ox}}$ is shown as a thick broken line. The arrows indicate the directions of the absorbance changes at the respective wavelength. The inset shows the spectrum of

each kinetic component resulting from global analysis of the transient spectra with a single-step sequential reaction model $[A \rightarrow B]$. (f) The time course of A_{457} after mixing $\Delta Y326$ $CtFNR_{red}$ with $NADP^+$. The measurement conditions were the same as those in Fig. 3e, except the $NADP^+$ concentrations of 0 μM (trace a), 100 μM (trace b), 200 μM (trace c) and 500 μM (trace d). The data are an average of four to five measurements. The fitted curves with a function of single exponential component are indicated as red lines. The residuals are indicated with black lines in the lower figure panel.

Fig. 4. (a) Transient spectra induced by mixing 9.3 μM $\Delta S338$ $CtFNR_{ox}$ with 100 μM $NADPH$. The reaction was performed in 20 mM HEPES-NaOH buffer (pH 7.0) at 10°C. The thin continuous lines from the top to the bottom at 450 nm indicated the spectra at 1 ms, 9 ms, 99 ms, 999 ms and 3999 ms, respectively. The spectra shown by thin dotted lines from the top to the bottom at 450 nm correspond to those at 4 ms, 19 ms, 49 ms, 199 ms, 499 ms and 1999 ms, respectively. The spectrum of $\Delta S338$ $CtFNR_{ox}$ in the absence of $NADPH$ is shown as a thick continuous line. The spectrum of $\Delta S338$ $CtFNR_{red}$ is shown as a thick broken line. The arrows indicate the directions of the absorbance changes at the respective wavelengths. The dashed parts of the arrows indicate change that occurred within the first data acquisition period (1 ms). The inset shows the spectrum of each kinetic component resulting from global analysis of the transient spectra with three-step sequential reaction model ($A \rightarrow B \rightarrow C \rightarrow D$ [fast/moderate/slow]). (b) The time course of A_{457} after mixing $\Delta S338$ $CtFNR_{ox}$ with $NADPH$ and $S-NADPD$. The measurement conditions were the same as those in Fig. 4a except the $NADPH$ concentrations of 0 μM (trace a), 100 μM (trace b), 200 μM (trace c) and 500 μM (trace d). The data are an average of four to five measurements. The time course of A_{457} after mixing $\Delta S338$ $CtFNR_{ox}$ with 100 μM $S-NADPD$ is shown as trace e with normalized FNR concentration. The fitted curves with a function of two exponential (trace b-d) and three exponential (trace e) components are indicated as red lines. The residuals are indicated as black lines ($NADPH$) and a red line ($S-NADPD$) in the lower figure panel. (c) Transient spectra induced by mixing 11.7 μM $\Delta S338$ $CtFNR_{red}$ with 100 μM $NADP^+$. The reaction was performed in 20 mM HEPES-NaOH buffer (pH 7.0) at 10°C. The spectra at 1 ms, 99 ms, 999 ms and 3999 ms are shown as thin continuous lines from the bottom to the top at 450 nm. The spectra shown by thin dotted lines from the bottom to the top at 450 nm correspond to those at 19 ms, 49 ms, 199 ms, 499 ms and 1999 ms, respectively. The spectrum of $\Delta S338$ $CtFNR_{ox}$ is shown as a thick broken line. The arrows indicate the direction of the absorbance change at the respective wavelengths. The inset shows the spectrum of each kinetic component resulting from global analysis of the transient spectra with two-step sequential reaction model ($A \rightarrow B \rightarrow C$ [fast/slow]). (d) The time course of A_{457} after mixing $\Delta S338$ $CtFNR_{red}$ with $NADP^+$. The measurement conditions were the same as those in Fig. 4c except the $NADP^+$ concentrations of 0 μM (trace a), 100 μM (trace b), 200 μM (trace c) and 500 μM (trace d). The data are an average of four to five measurements. The

fitted curves with a function of two exponential components are indicated as red lines. The residuals are indicated as black lines in the lower figure panel.

Fig. 5 (a) Transient spectra induced by mixing 9.0 μM $\Delta\text{F337 CtFNR}_{\text{ox}}$ with 100 μM NADPH. The reaction was performed in 20 mM HEPES-NaOH buffer (pH 7.0) at 10°C. The thin continuous lines from the top to the bottom at 450 nm indicated the spectra at 1 ms, 9 ms, 99 ms and 999 ms, respectively. The spectra shown by thin dotted lines from the top to the bottom at 450 nm correspond to those at 4 ms, 19 ms, 49 ms, 199 ms, 499 ms, 1999 ms and 3999 ms, respectively. The spectrum of $\Delta\text{F337 CtFNR}_{\text{ox}}$ in the absence of NADPH is shown as a thick continuous line. The arrows indicate the directions of the absorbance changes at the respective wavelengths. The dashed parts of the arrows indicate changes that occurred within the first data acquisition period (1 ms). The inset shows the spectra of kinetic components resulting from global analysis of the transient spectra with two-step sequential reaction model ($A \rightarrow B \rightarrow C$ [fast/slow]). (b) The time course of A_{457} after mixing $\Delta\text{F337 CtFNR}_{\text{ox}}$ with NADPH and *S*-NADPD. The measurement conditions were the same as those in Fig. 5a except the NADPH concentrations of 0 μM (trace a), 100 μM (trace b), 200 μM (trace c) and 500 μM (trace d). The data are an average of four to five measurements. The time course of A_{457} after mixing $\Delta\text{F337 CtFNR}_{\text{ox}}$ with 100 μM *S*-NADPD is shown as trace e with normalized FNR concentration. The fitted curves with functions of two exponential (trace b-d) and three exponential (trace e) components are indicated as red lines. The residuals are indicated as black lines (NADPH) and a red line (*S*-NADPD) in the lower figure panel.

Table 1Enzymatic, spectroscopic and molecular mass properties of WT, Δ Y326, Δ F337 and Δ S338 CtfNRs.

	WT	Δ Y326	Δ F337	Δ S338
NADPH diaphorase with ferricyanide^a				
K_m for NADPH (μ M)	14.2 \pm 0.9	9.9 \pm 0.5	10.2 \pm 0.4	10.9 \pm 0.6
k_{cat} (s^{-1})	213 \pm 3	190 \pm 2	161 \pm 1.3	172 \pm 2
k_{cat}/K_m ($\times 10^6$ M ⁻¹ s ⁻¹)	15.0 \pm 0.2	19.2 \pm 0.2	15.8 \pm 0.13	15.8 \pm 0.18
K_d for NADP ⁺ (μ M) ^b	7.6 \pm 0.4	12.5 \pm 0.4	11.5 \pm 1.3	13.6 \pm 0.3
ϵ (mM ⁻¹ cm ⁻¹ per subunit) / at λ max (nm)	10.3/ 466 ^c	10.3/ 457	10.6 / 457	10.3/ 458
M_r (gel-permeation/ SDS-PAGE)(kDa)	91 / 42	68 / 38	66 / 39	71 / 39

Parameter values with \pm one standard deviation are represented.

a: with 2 mM ferricyanide in 20 mM HEPES-NaOH buffer (pH 7.0) at 25°C.

b: obtained with the data in Figure 2c.

c: from Seo and Sakurai (2002)

Table 2Kinetic constants obtained by the pre-steady-state analysis of the reaction of $\Delta Y326 CtfNR_{ox}$ with NADPH.

[NADPH] (μM)	100 ^a	200 ^a	300	500 ^a	25 ^b
k_1 (s^{-1})	154 \pm 3 (100 \pm 15)	208 \pm 5 (137 \pm 23)	186 \pm 5 (123 \pm 17)	205 \pm 5 (140 \pm 30)	117 \pm 1.8 (99 \pm 10)
ΔA_1	0.0170 \pm 0.0002	0.0140 \pm 0.0002	0.0146 \pm 0.0002	0.0124 \pm 0.00017	0.0468 \pm 0.0004
k_2 (s^{-1})	25.2 \pm 0.3 (18.5 \pm 1.6)	29.6 \pm 0.2 (26.7 \pm 1.3)	28.5 \pm 0.3 (24 \pm 1.6)	28.7 \pm 0.19 (27 \pm 1.8)	-
ΔA_2	0.0237 \pm 0.0002	0.0277 \pm 0.0001	0.0301 \pm 0.0002	0.0322 \pm 0.00013	-
k_3 (s^{-1})	2.95 \pm 0.02 (2.6 \pm 0.3)	3.47 \pm 0.02 (3.6 \pm 0.13)	3.51 \pm 0.02 (3.3 \pm 0.2)	3.53 \pm 0.019 (3.6 \pm 0.17)	3.06 \pm 0.01 (3.2 \pm 0.2)
ΔA_3	0.01815 \pm 0.00006	0.01834 \pm 0.00006	0.01832 \pm 0.00007	0.01797 \pm 0.00006	0.07764 \pm 0.00009

Rate constants (k) and amplitudes (ΔA) of each kinetic component obtained by fitting with bi- or tri-exponential decay functions against absorption changes at 457 nm at 0-1000 ms time period are represented in the order from the fastest to the slowest. Measurement conditions are described in legends of Fig. 3b and 3d. The value of each parameter is represented with \pm one standard deviation. The rate constant values in the parentheses are those obtained by global analysis of the transition of absorptions with a three-step reaction model ($A \rightarrow B \rightarrow C \rightarrow D$ [fast/moderate/slow]) for 100-500 μM NADPH or a two-step reaction model ($A \rightarrow B \rightarrow C$ [fast/slow]) for 25 μM NADPH.

a: mixing with 9.3 μM $\Delta Y326 CtfNR_{ox}$ with NADPH. Data in Fig.3b were utilized for the estimation.

b: mixing with 25 μM $\Delta Y326 CtfNR_{ox}$ with 25 μM NADPH. Data in Fig.3d were utilized for the estimation.

Table 3Kinetic constants obtained by the pre-steady-state analysis of the reaction of Δ S338 *CtFNR*_{ox} with NADPH.

[NADPH] (μ M)	100 ^a	200 ^a	300	500 ^a
k_1 (s^{-1})	50.0 \pm 0.4	43.4 \pm 0.3	37.5 \pm 0.2	36.2 \pm 0.4
	(810 \pm 80, 47 \pm 6)	(530 \pm 90, 37 \pm 7)	(270 \pm 70, 35 \pm 3)	(360 \pm 80, 30 \pm 2)
ΔA_1	0.01570 \pm 0.00008	0.01777 \pm 0.00006	0.02116 \pm 0.0006	0.0209 \pm 0.0001
k_2 (s^{-1})	1.34 \pm 0.04 (1.1 \pm 0.5)	1.01 \pm 0.03 (1.1 \pm 0.17)	0.82 \pm 0.03 (0.68 \pm 0.09)	1.55 \pm 0.06 (0.4 \pm 0.5)
	0.00637 \pm 0.00008	0.0084 \pm 0.00014	0.0106 \pm 0.0003	0.00788 \pm 0.00009

Rate constants (k) and amplitudes (ΔA) of each kinetic component obtained by fitting with bi-exponential decay functions against absorption changes at 457 nm at 0 ms – 1000 ms time region are represented in the order from the fastest to the slowest. Measurement conditions are described in legends of Fig.4b. The value of each parameter is represented with \pm one standard deviation. The rate constant values in the parentheses are those obtained by global analysis of the transition of absorptions with a three-step reaction model ($A \rightarrow B \rightarrow C \rightarrow D$ [fast/moderate/slow]). The rate constants of fastest and middle phase are indicated in the same parentheses in k_1 column. Slowest one is indicated in k_2 column.

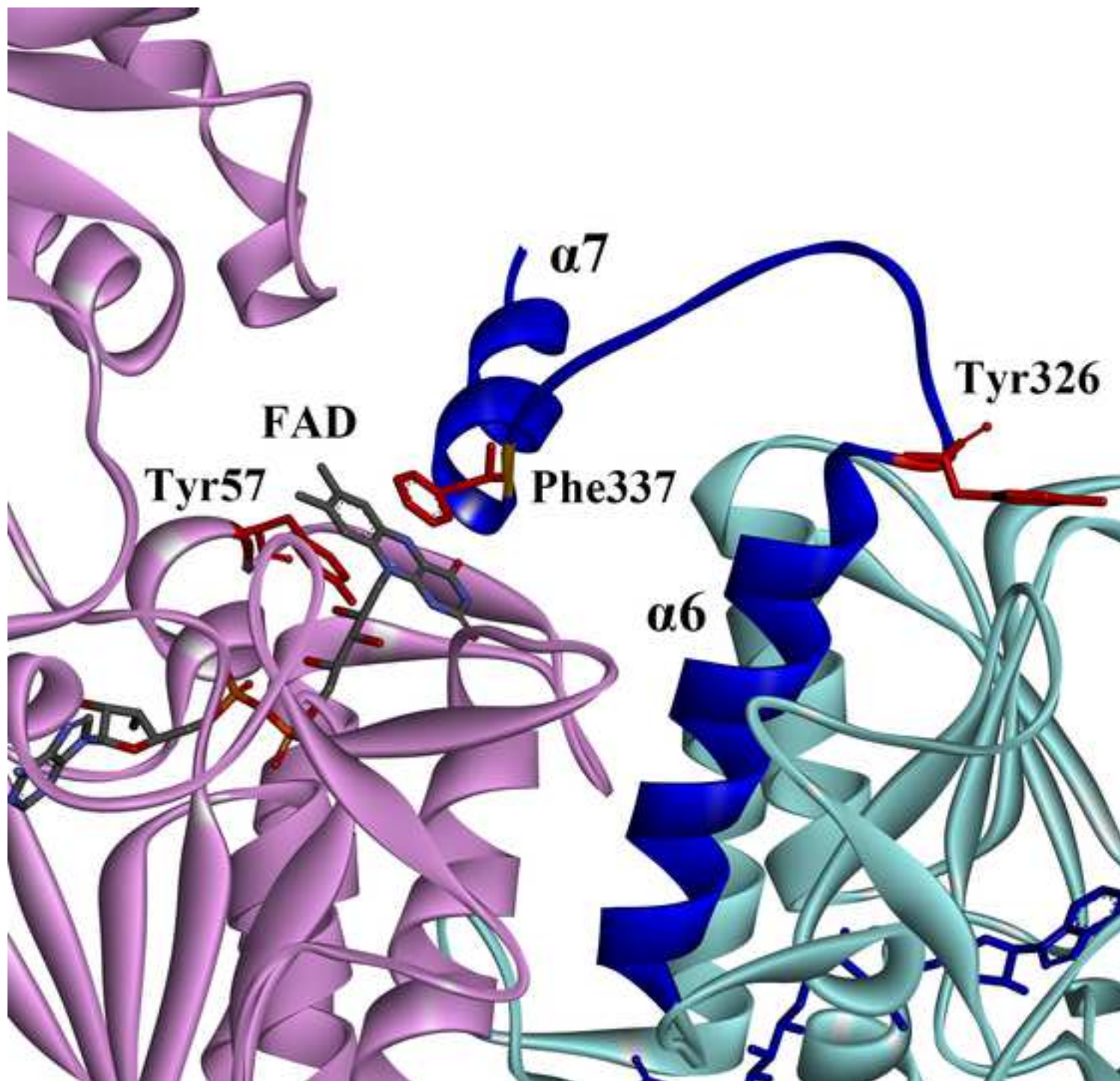
a: mixing with 9.3 μ M Δ S338 *CtFNR*_{ox} with NADPH. Data in Fig.4b were utilized for the estimation.

Table 4Kinetic constants obtained by the pre-steady-state analysis of the reaction of $\Delta F337$ CtfNR_{ox} with NADPH.

[NADPH] (μ M)	100 ^a	200 ^a	500 ^a
k_1 (s^{-1})	41.8 \pm 0.4 (50 \pm 3)	37.5 \pm 0.3 (42 \pm 1.8)	30.5 \pm 0.16 (30 \pm 1.2)
ΔA_1	0.0177 \pm 0.0001	0.02083 \pm 0.00007	0.02410 \pm 0.00006
k_2 (s^{-1})	1.69 \pm 0.07 (2.2 \pm 0.13)	1.39 \pm 0.05 (1.6 \pm 0.15)	0.98 \pm 0.04 (0.69 \pm 0.09)
ΔA_2	0.00555 \pm 0.00007	0.00627 \pm 0.00008	0.0080 \pm 0.00018

Rate constants (k) and amplitudes (ΔA) of each kinetic component obtained by fitting with a bi-exponential decay functions against absorption changes at 457 nm are represented in the order from the fastest to the slowest. Measurement conditions are described in legends of Fig.5b. The value of each parameter is represented with \pm one standard deviation. The rate constant values in the parentheses are those obtained from global analysis of the transition of absorptions with a two-step reaction model (A \rightarrow B \rightarrow C [fast/slow]).

a: mixing with 9.0 μ M $\Delta F337$ CtfNR_{ox} with NADPH. Data in Figure 5b were utilized for the estimation.



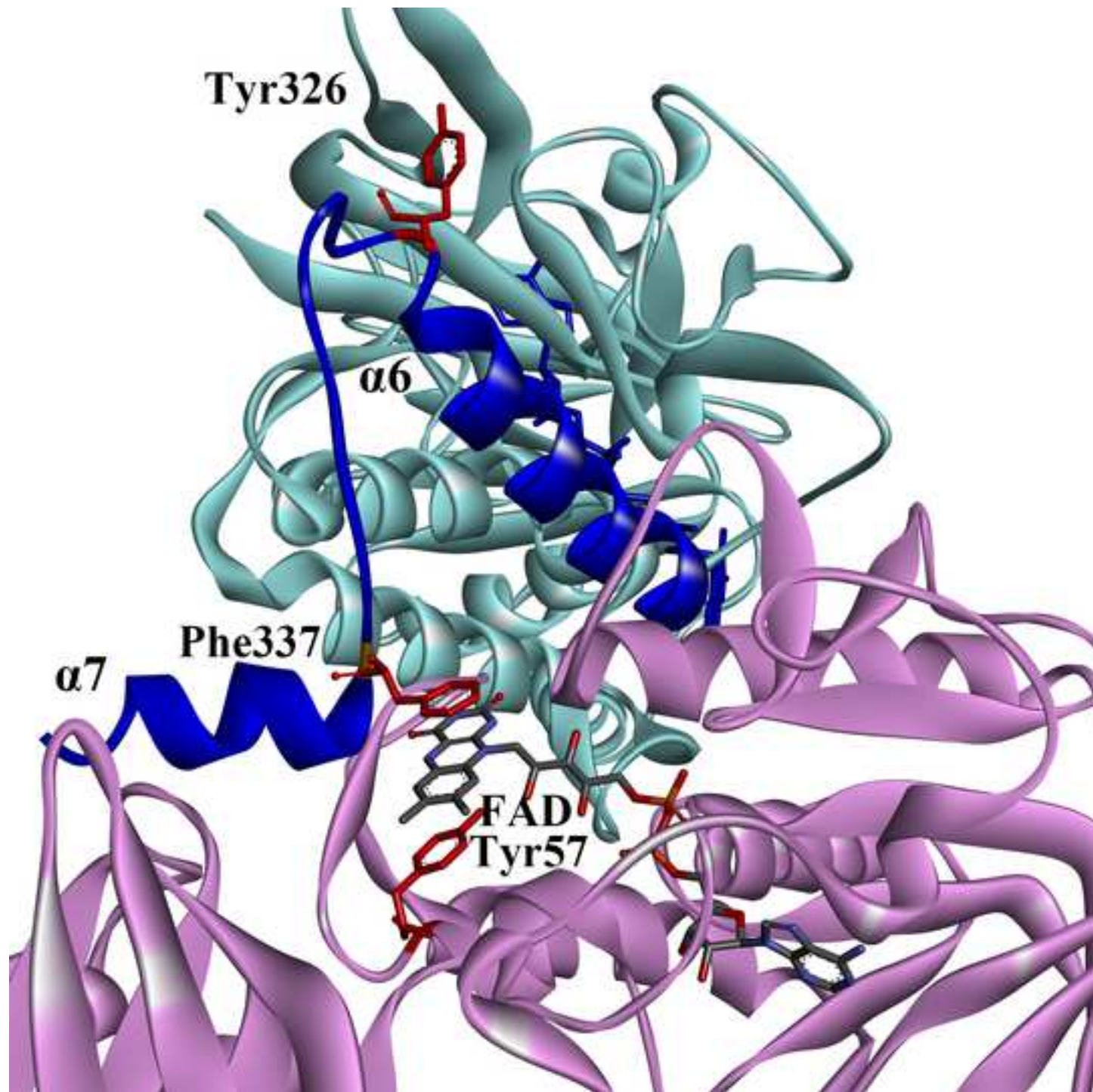


Figure 1c

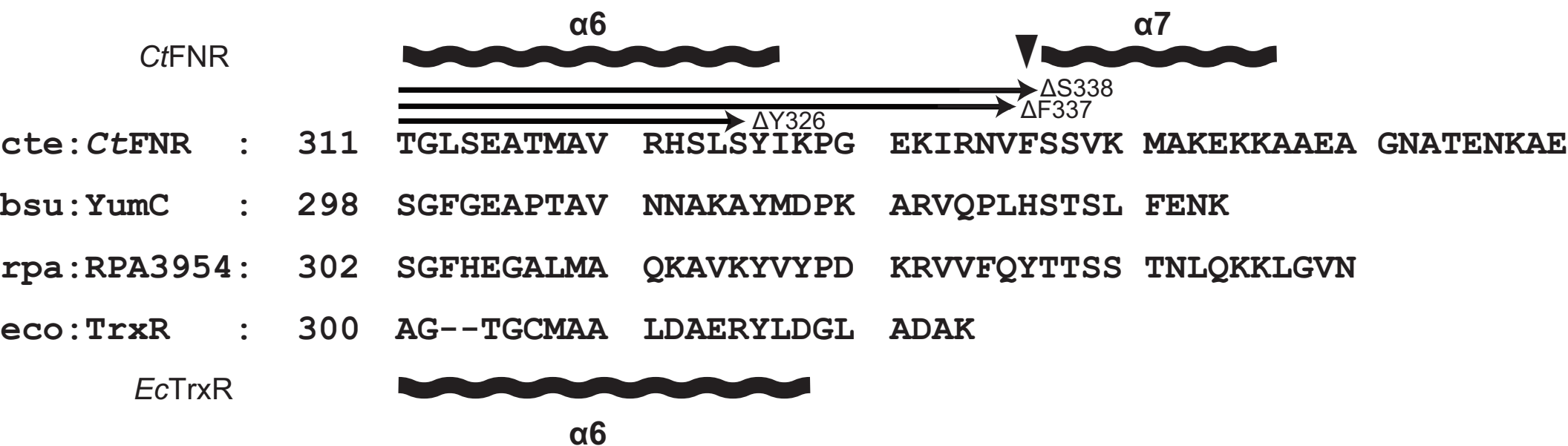


Figure 2a
Figure 2a

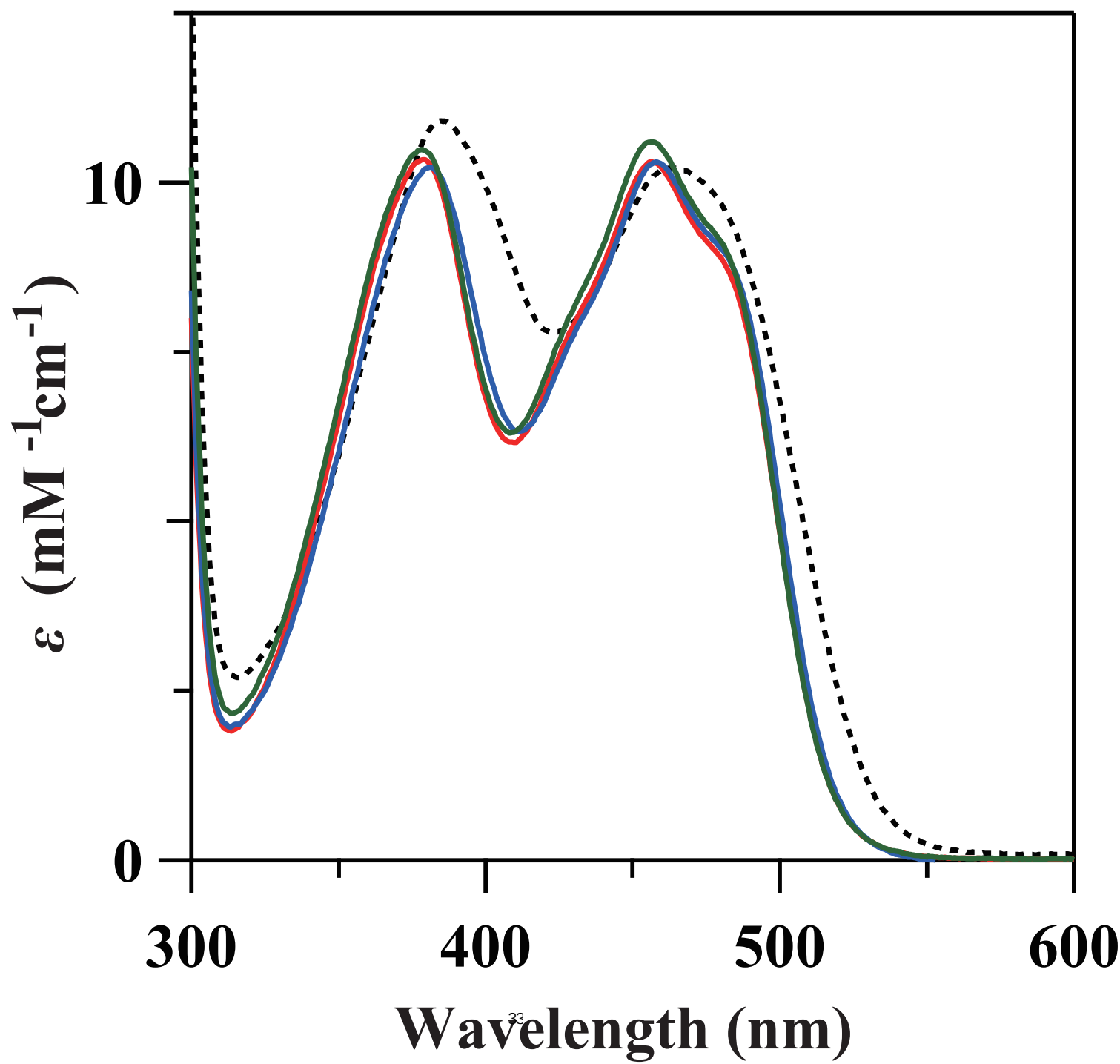


Figure 2b

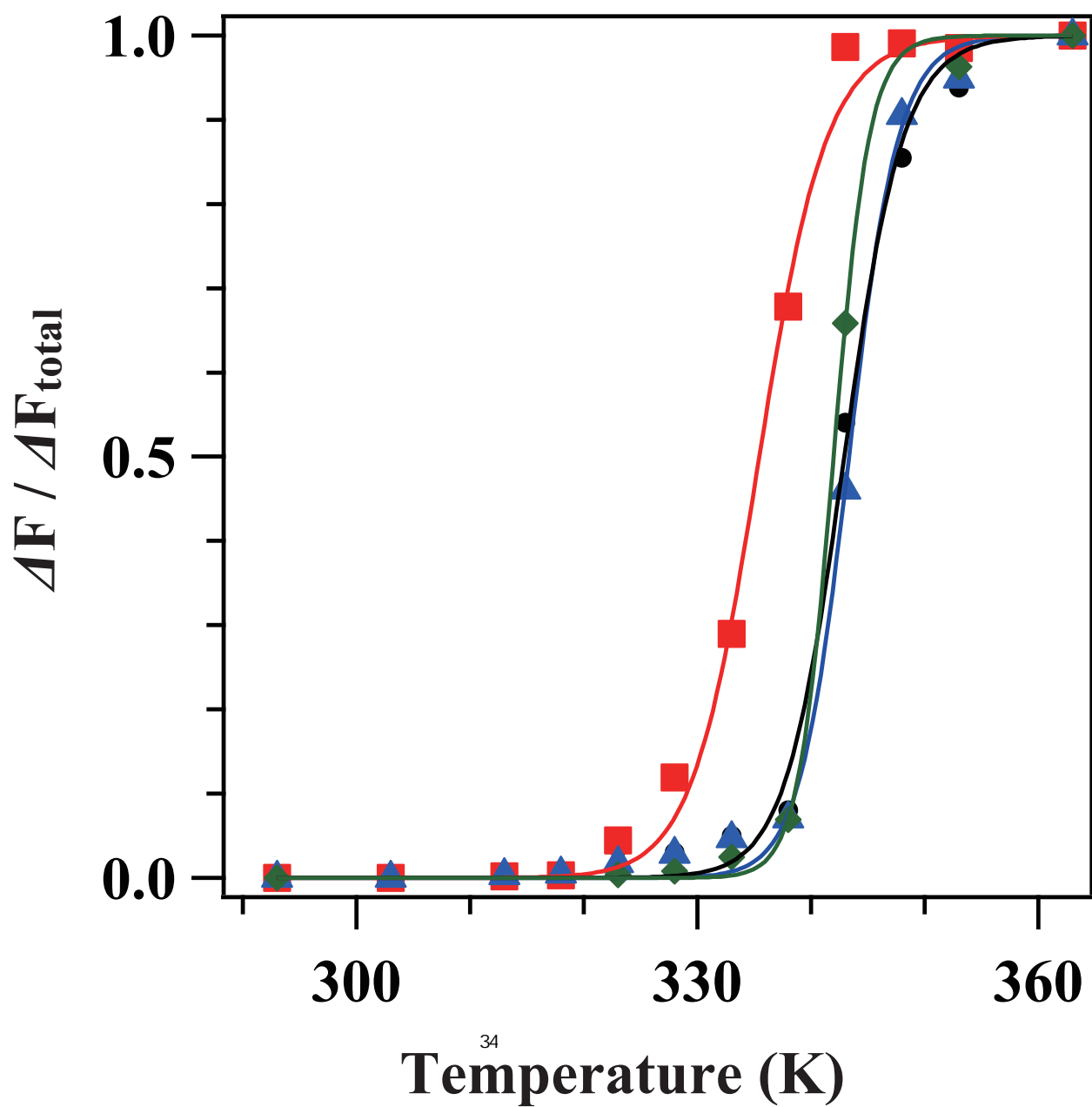


Figure 2c

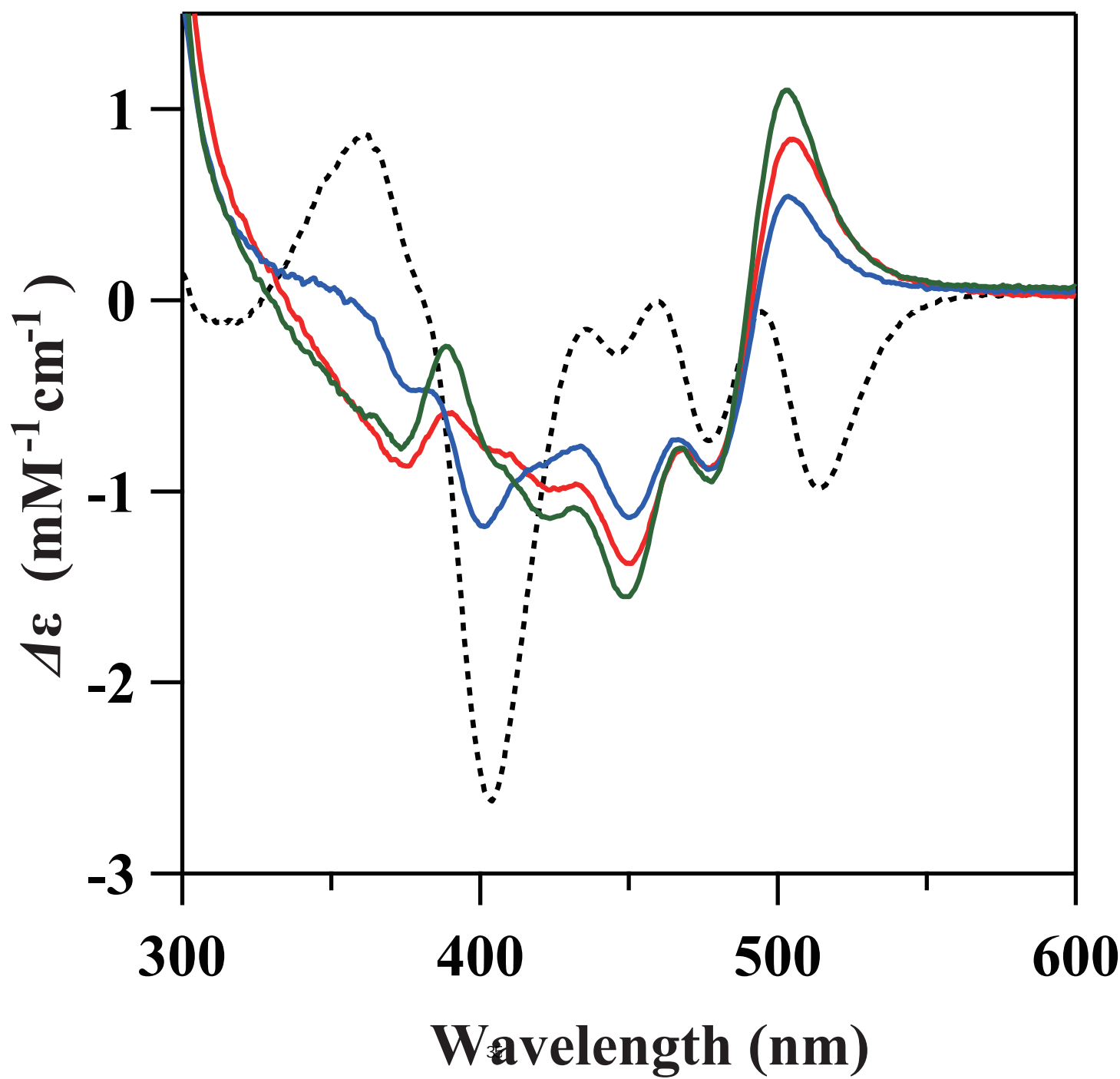


Figure 2d

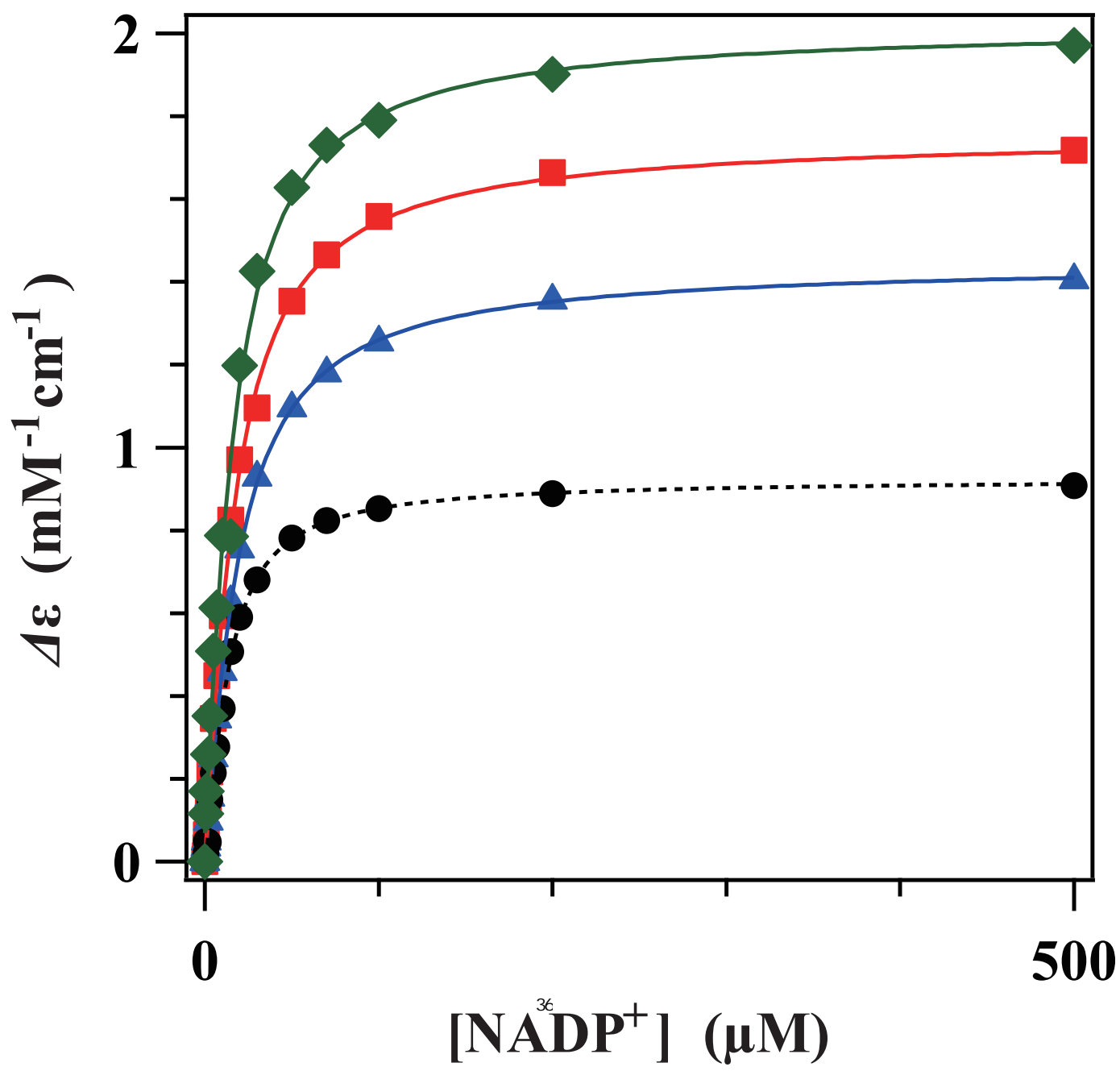
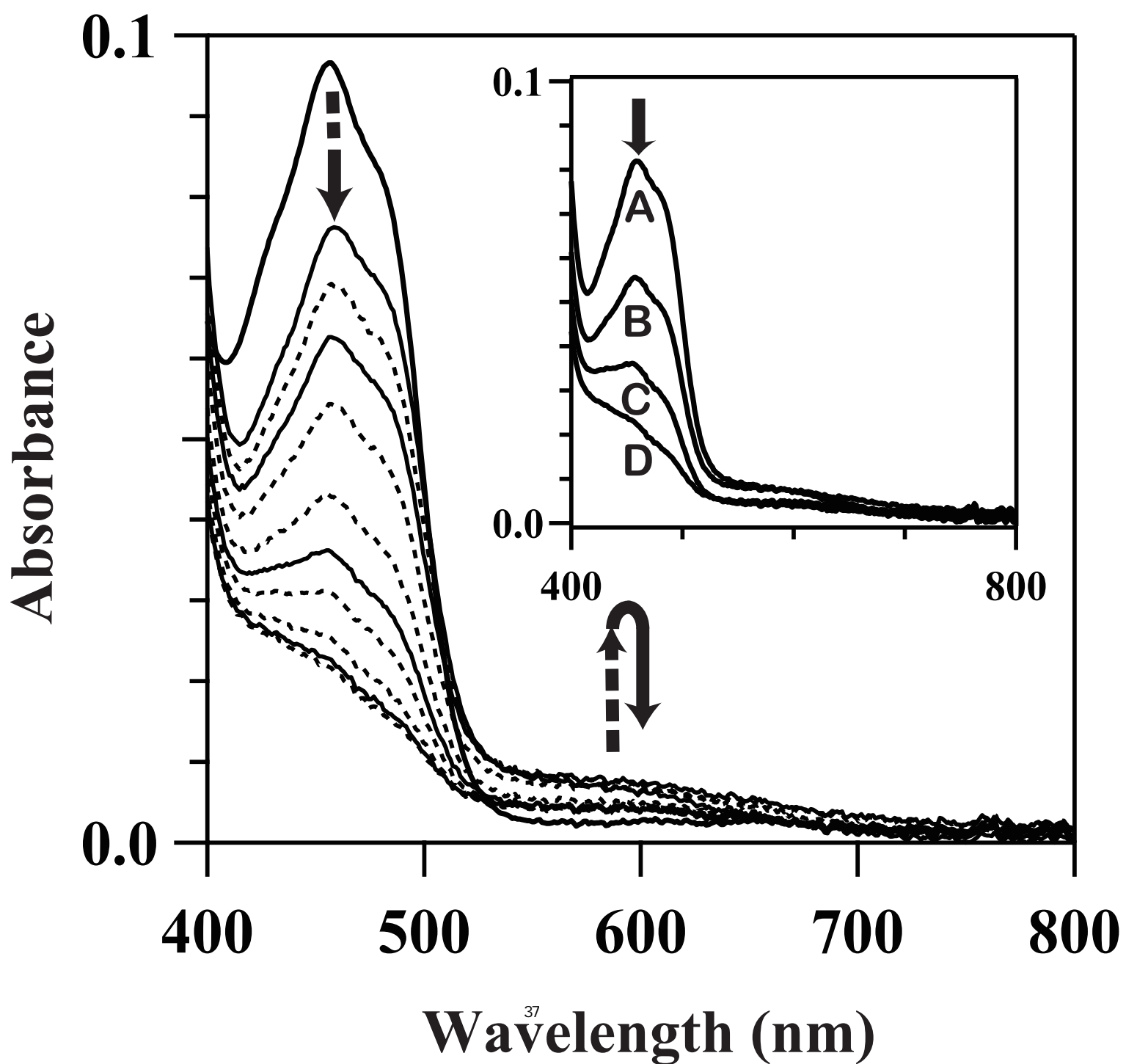


Figure 3a



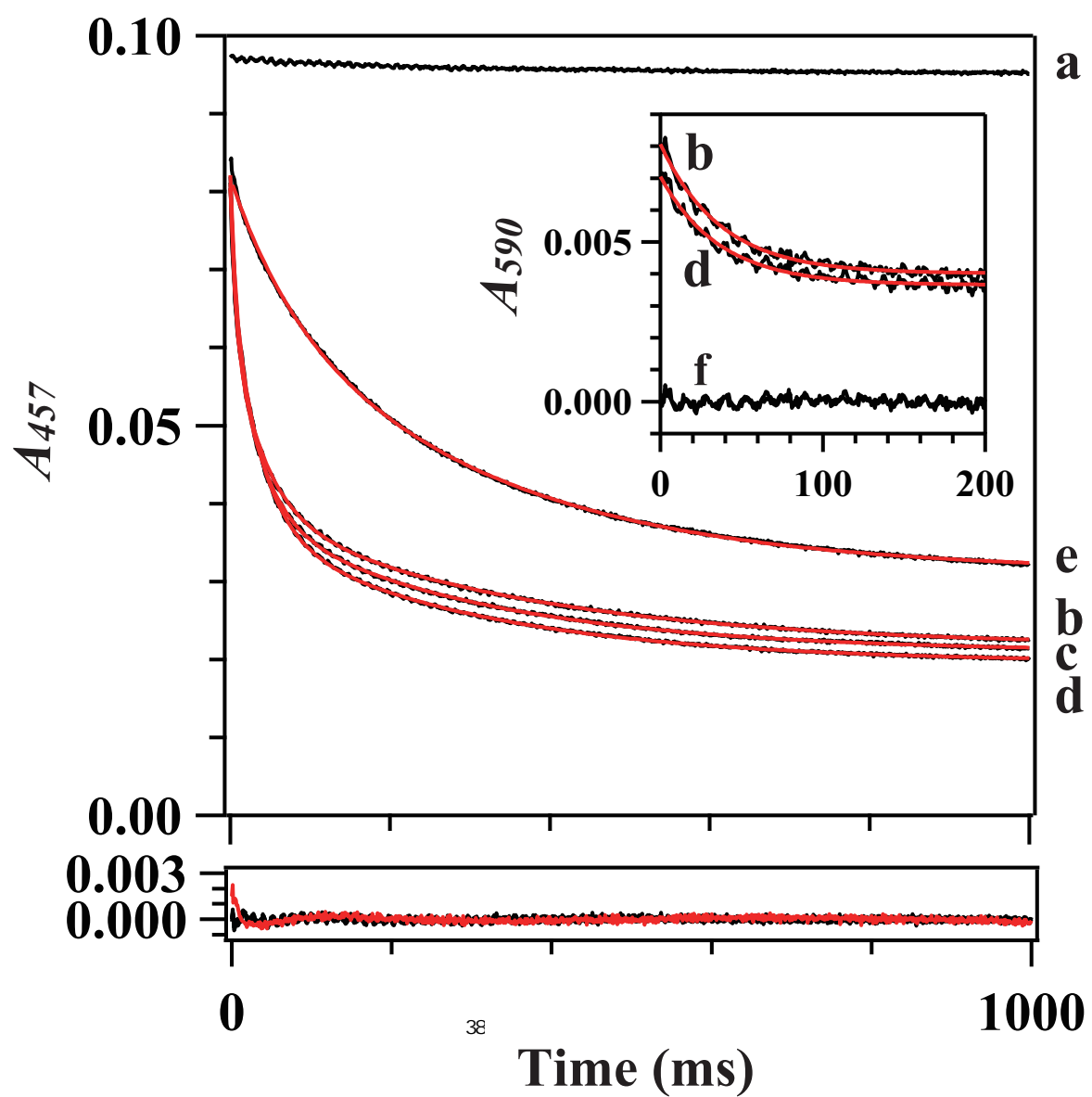


Figure 3c

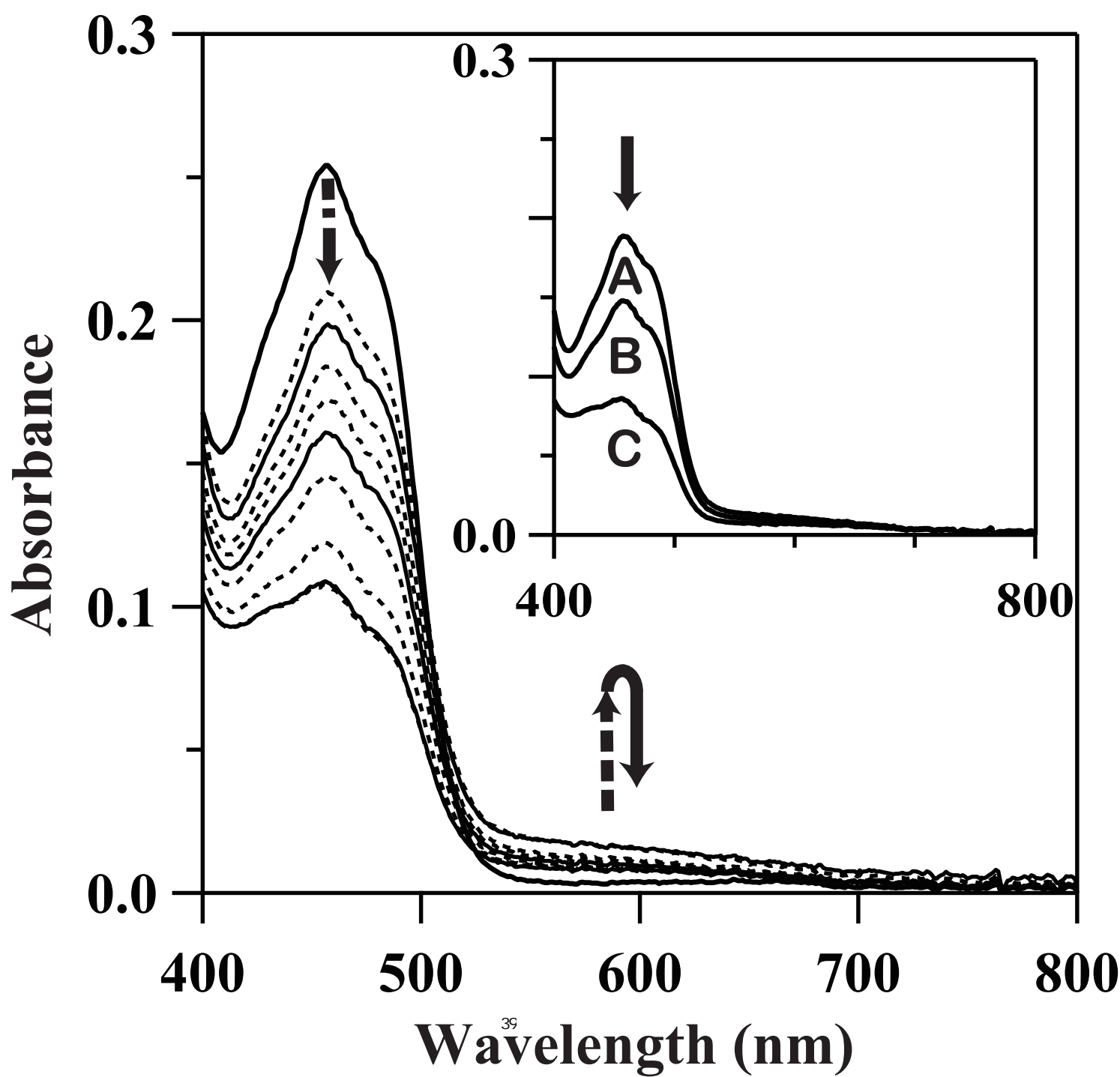


Figure 3d

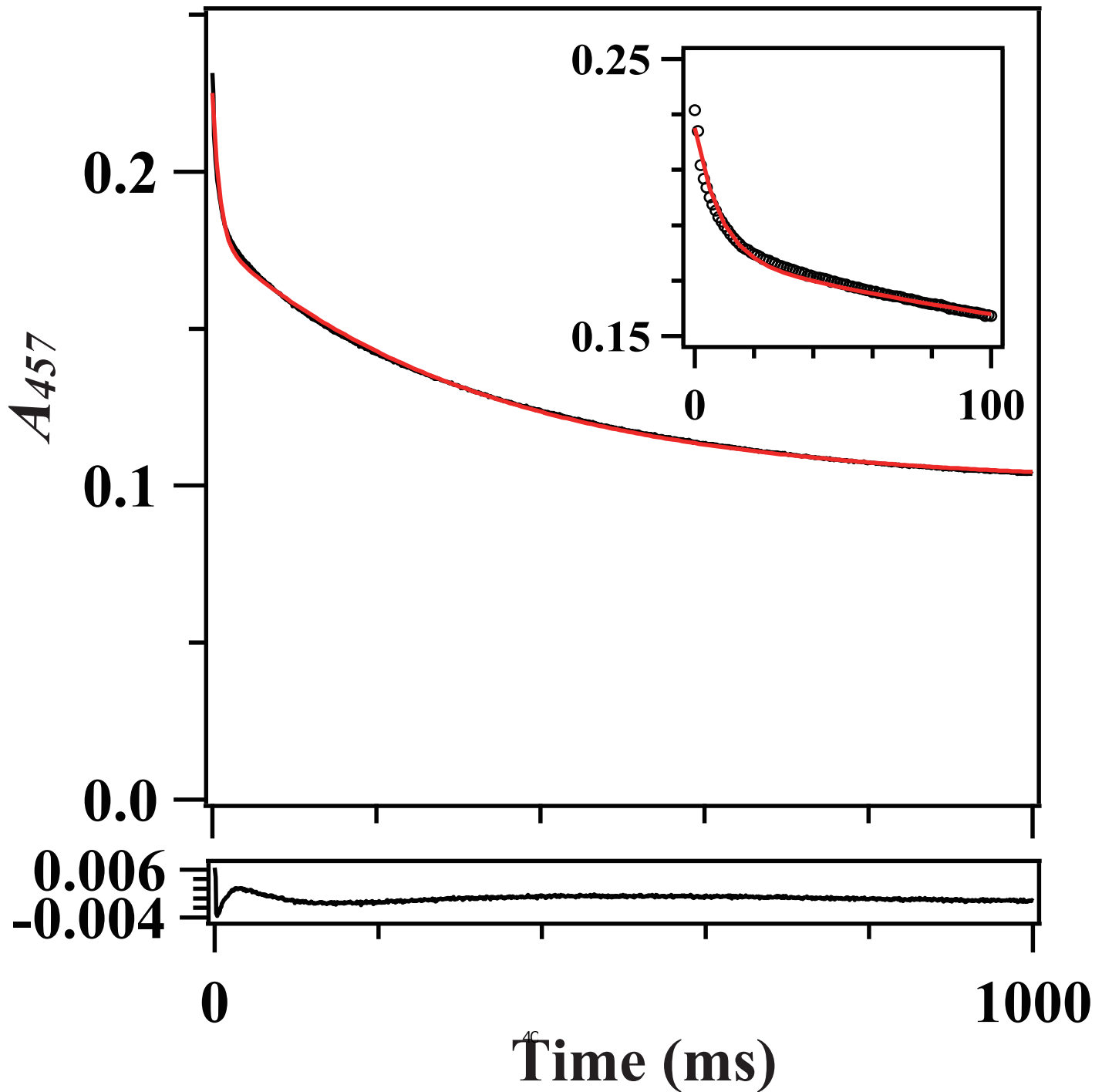


Figure 3e

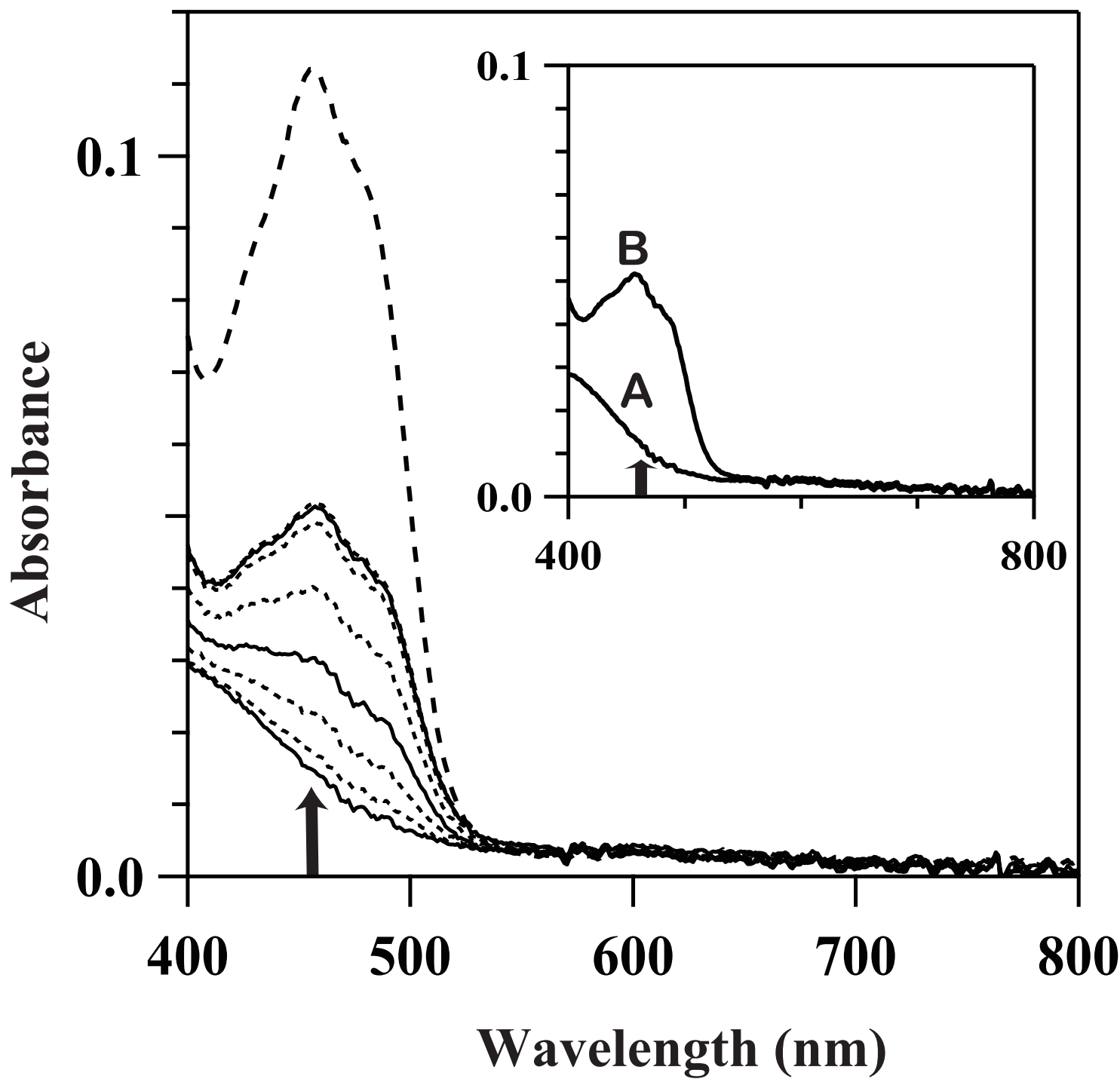


Figure 3f

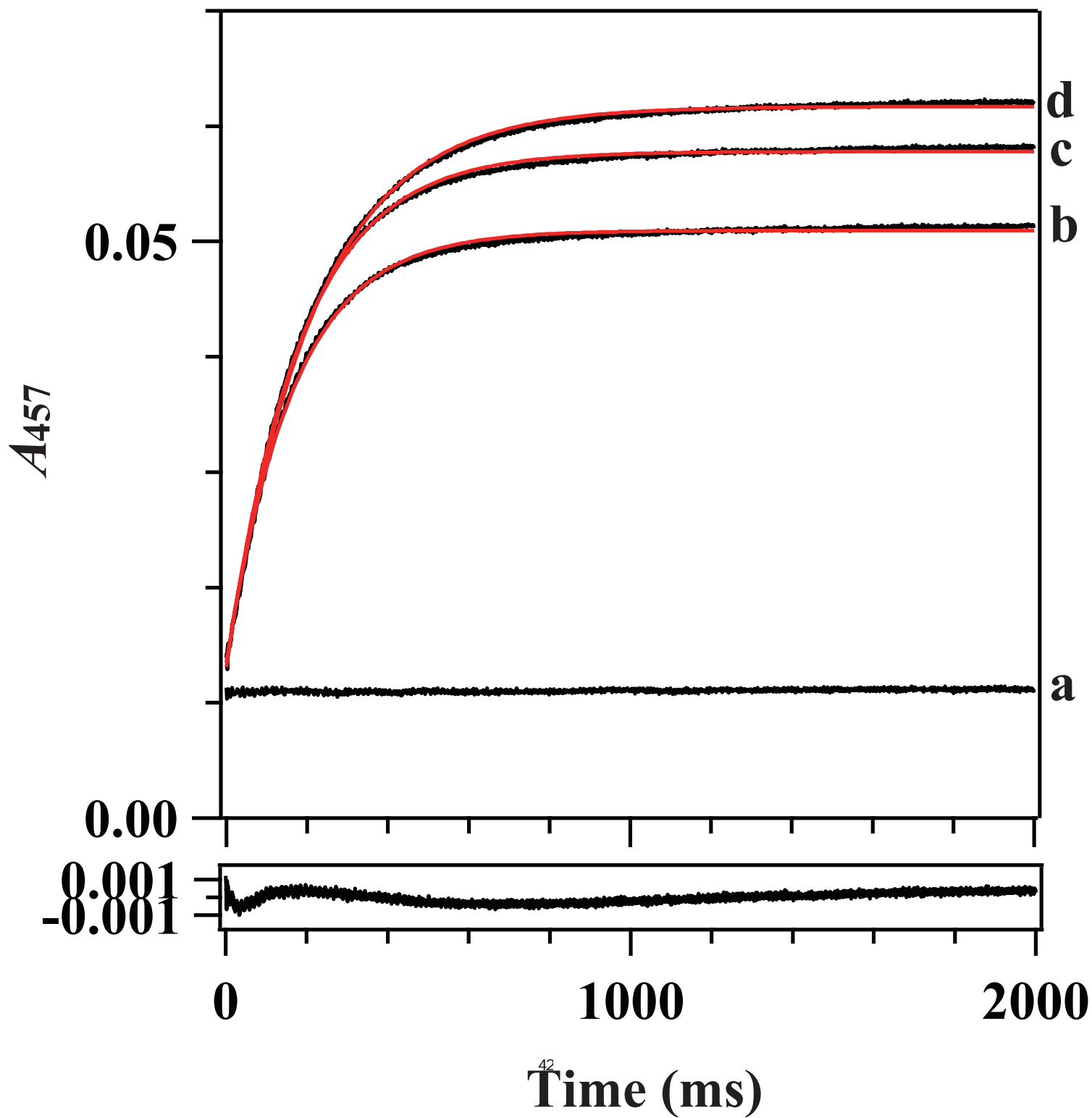
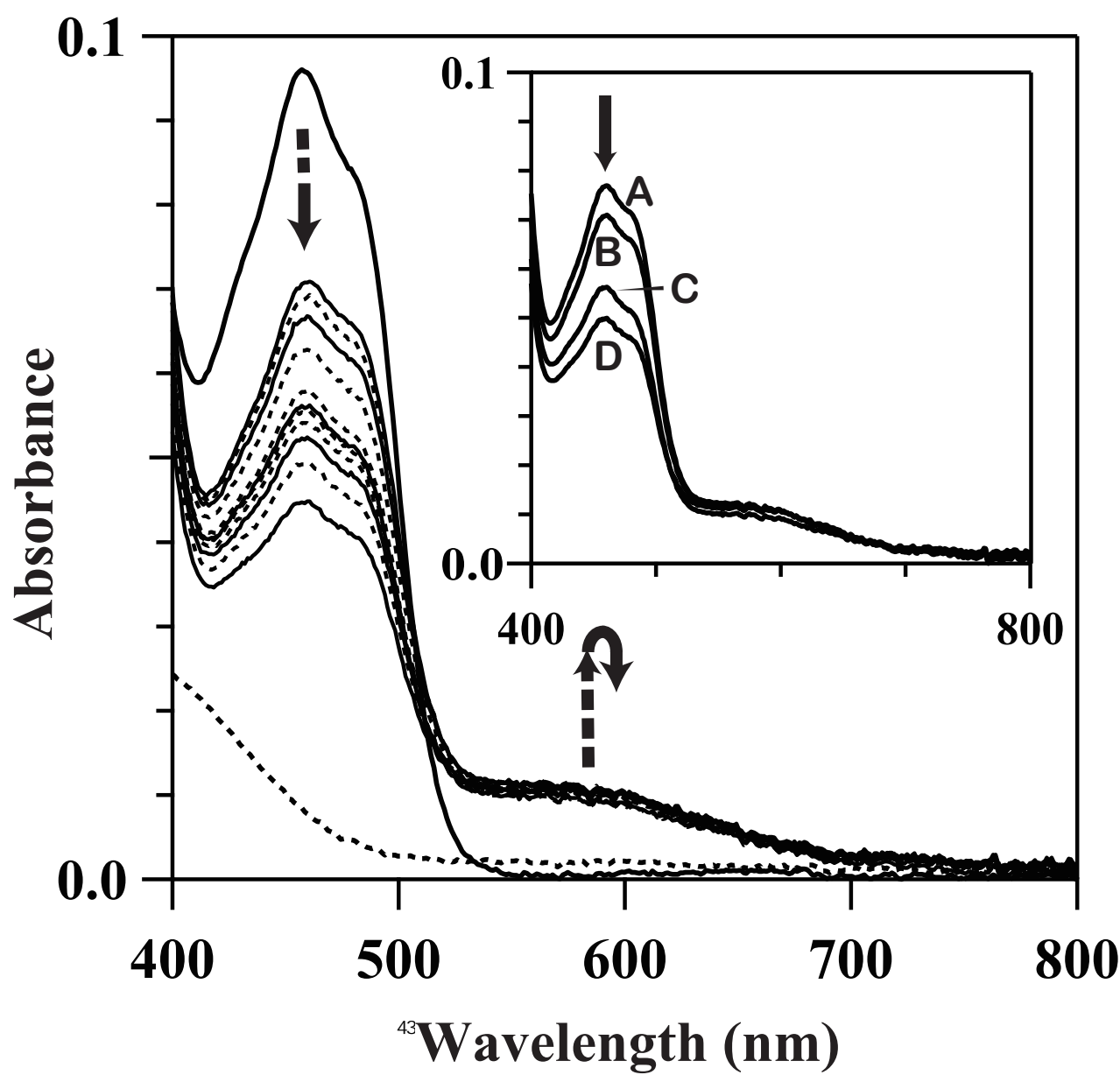


Figure 4a



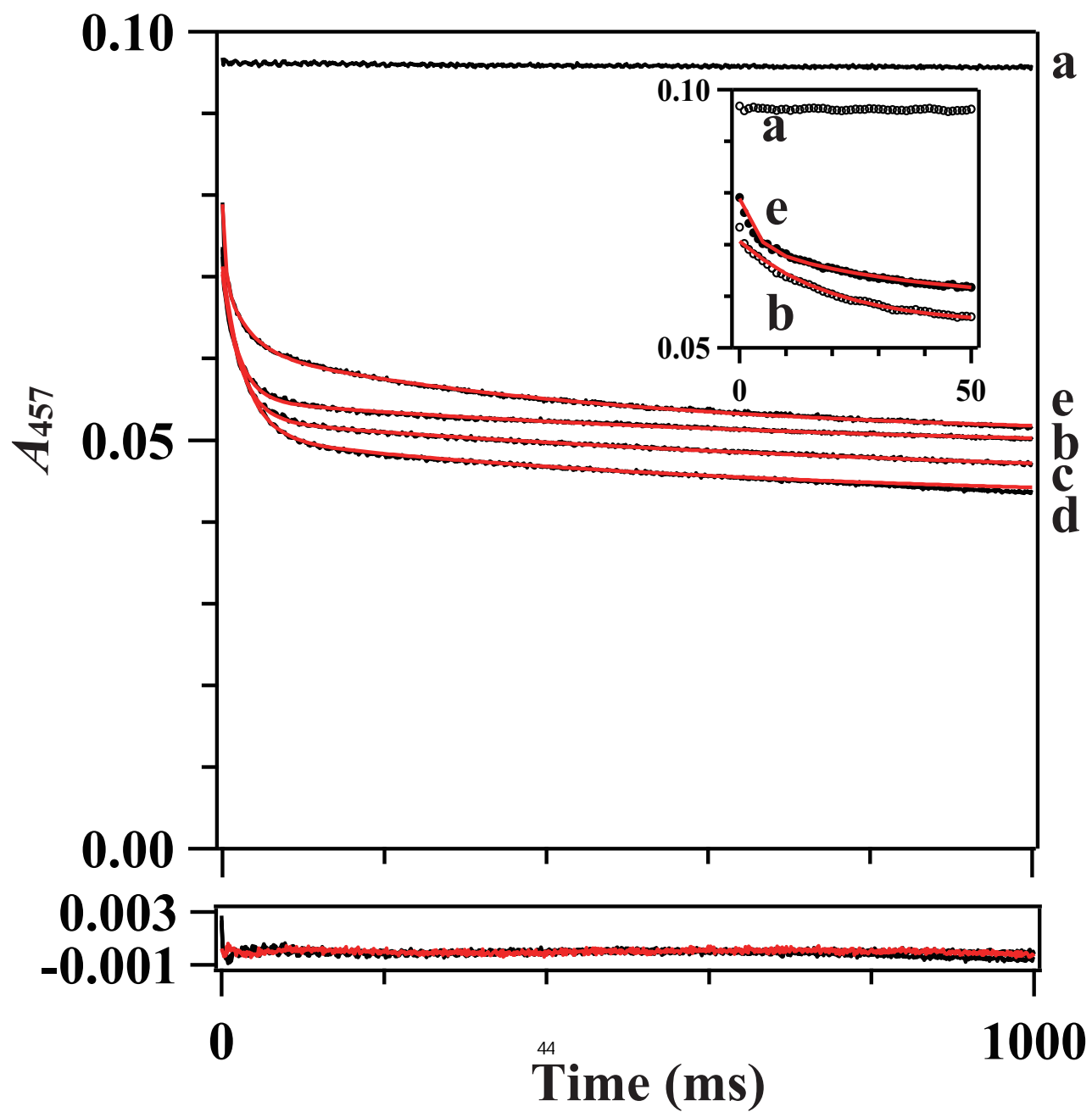
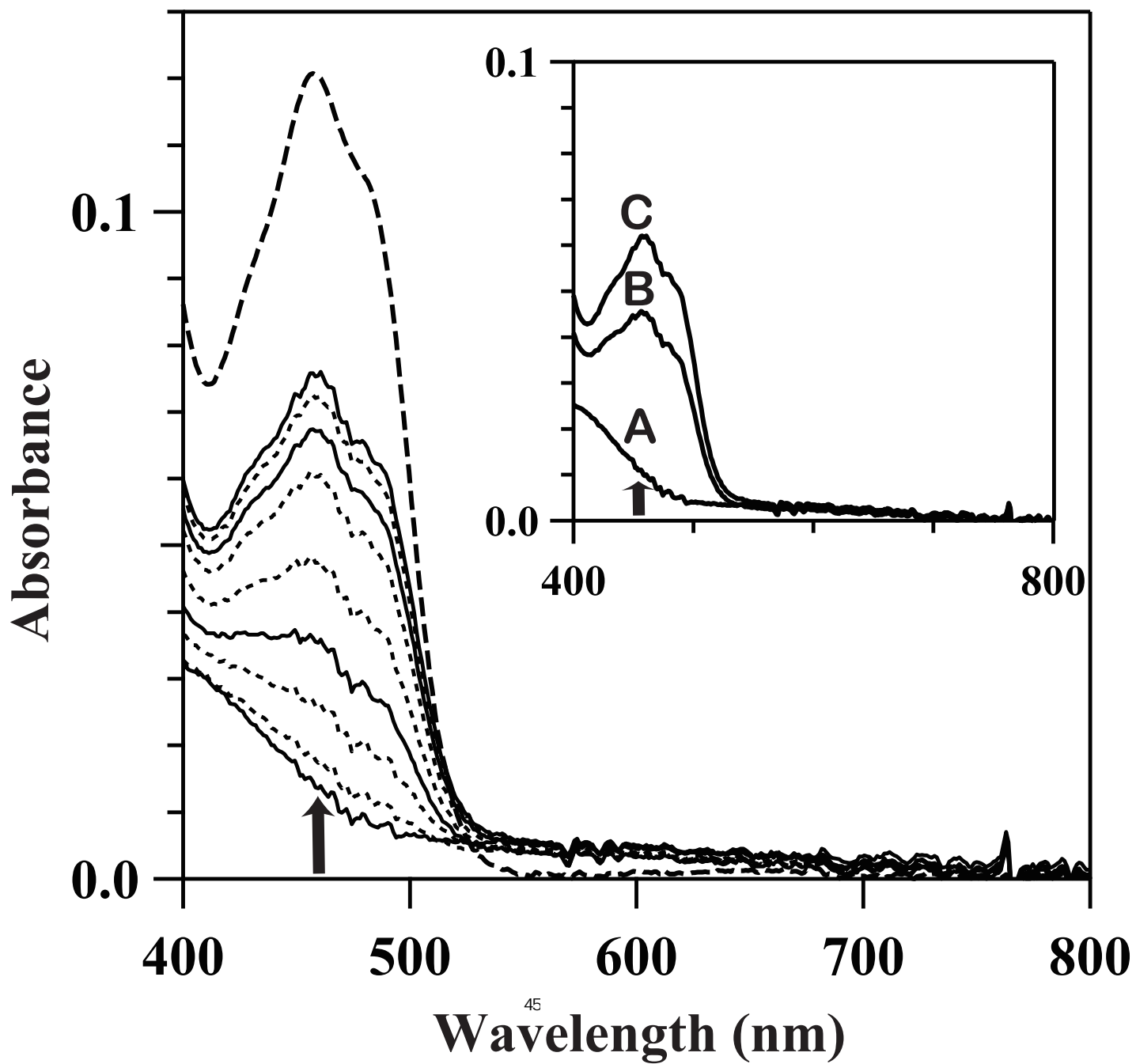


Figure 4c



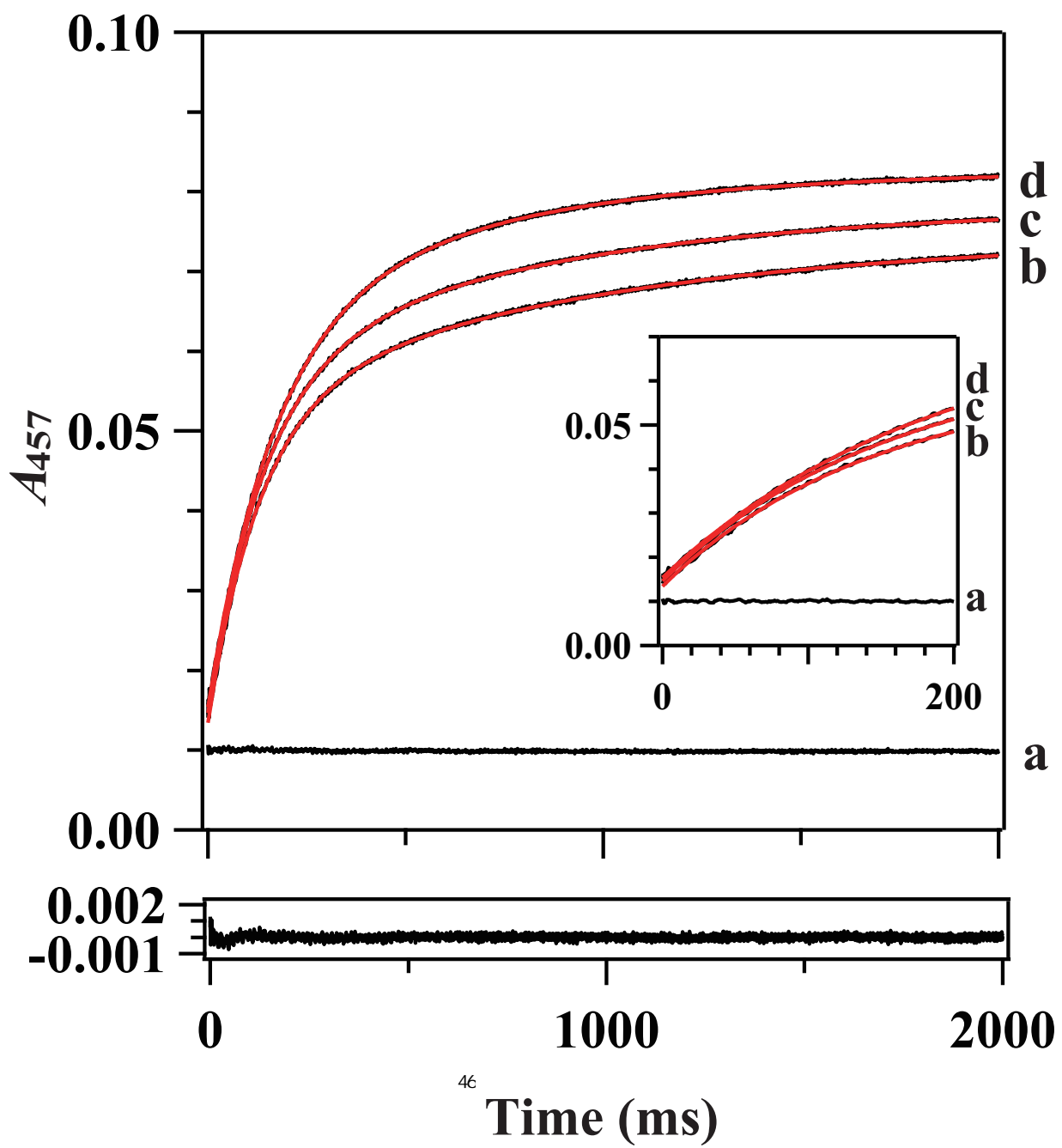


Figure 5a

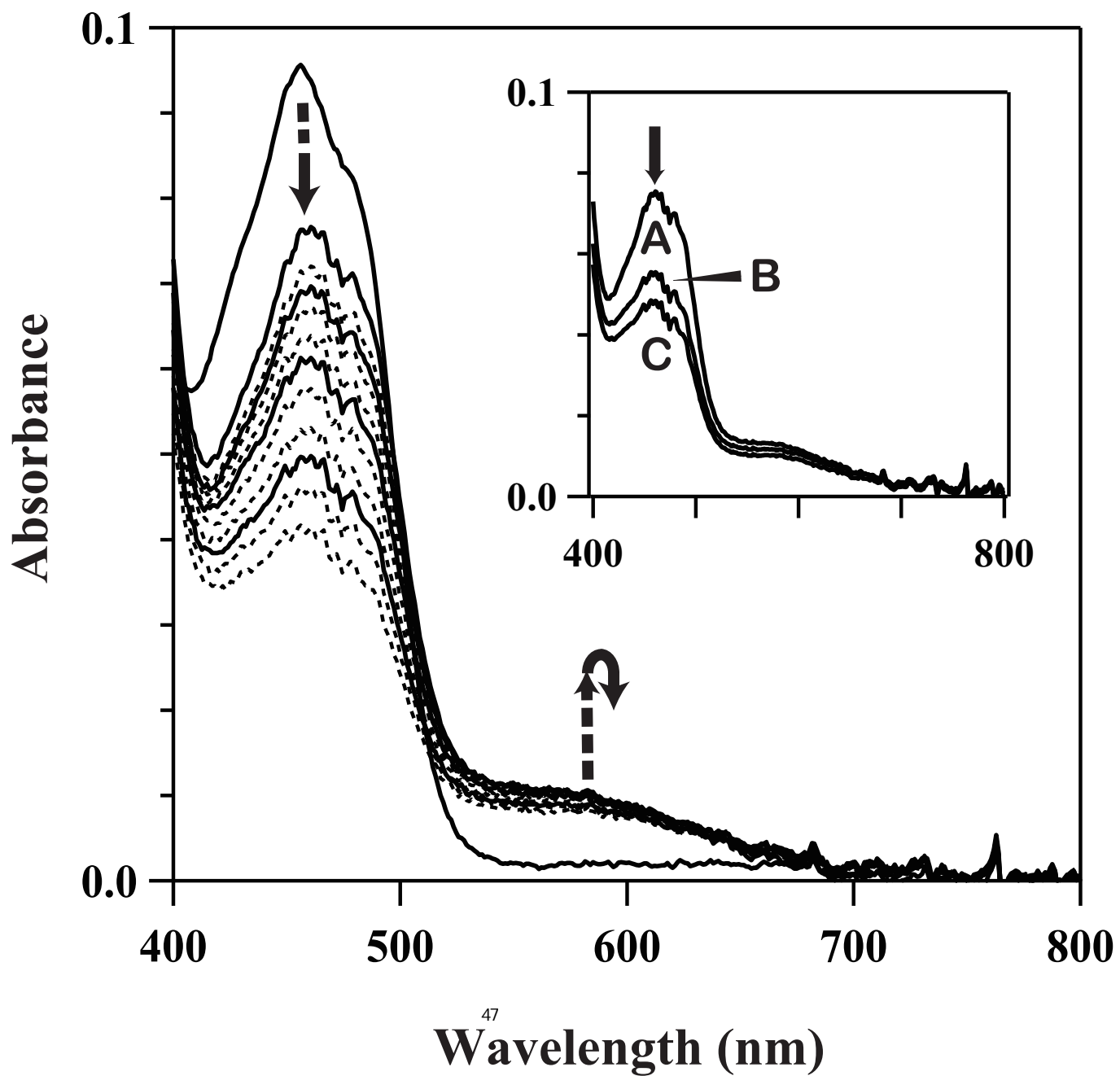


Figure 5b

